國立彰化師範大學光電科技研究所

碩士論文

指導教授：郭艷光博士

850-nm 面射型雷射應力量子井結構之模擬與分析

Numerical Study on Strained Quantum-Well Structures for 850-nm Vertical-Cavity Surface-Emitting Lasers

研究生：陳俊榮撰

中華民國九十五年六月

國立彰化師範大學光電科技研究所

碩士論文

研究生：陳俊榮

850-nm 面射型雷射應力量子井結構之模擬與分析

Numerical Study on Strained Quantum-Well Structures for 850-nm Vertical-Cavity Surface-Emitting Lasers

本論文業經審查及口試合格特此證明

論文考試委員會主席：__________

委員：__________ __________ __________

指導教授：郭艷光教授__________

所長：洪連輝主任__________

中華民國九十五年六月

國立彰化師範大學

博碩士論文電子檔案上網授權書

（提供授權人裝釘於紙本論文審定頁之次頁用）

本授權書所授權之論文為授權人在 國立彰化師範 大學 光電科技 研究所 94 學年度第 二 學期取得 碩 士學位之論文。

論文題目： 850-nm 面射型雷射應力量子井結構之模擬與分析

指導教授： 郭艷光 教授

茲 同意將授權人擁有著作權之上列論文全文（含摘要），授權**本校圖書館及國家圖書館**，以電子檔上載網路等數位化方式，提供讀者基於個人非營利性質之線上檢索、閱覽、下載或列印。

論文電子全文上載網路公開時間：

一、校內區域網路：

☑ 立刻公開 ☐ 1 年後公開 ☐ 2 年後公開 ☐ 3 年後公開

☐ 4 年後公開 ☐ 5 年後公開 ☐ 不公開

二、校外網際網路：

☑ 立刻公開 ☐ 1 年後公開 ☐ 2 年後公開 ☐ 3 年後公開

☐ 4 年後公開 ☐ 5 年後公開 ☐ 不公開

指導教授：郭艷光 教授

研究生（授權人）簽名： （請親筆正楷簽名）

學 號：93252005

中 華 民 國 95 年 6 月 日

Acknowledgment

I would like to sincerely acknowledge my academic advisor, Professor Yen-Kuang Kuo. I have learned much knowledge in optoelectronics from his guidance. In addition, I think it is more important that I can learn the sense of responsibility and the serious attitude toward learning and research from him. He always supports the research ideas proposed by me and gives me great advice. By the way, he has a very famous Nano Band in Changhua.

Besides, I would like to thank Professor Man-Fang Huang. She always answers my questions friendly and kindly. She is conscientious about her teaching all the time, and I deeply respect her for that. Therefore, I always specially concentrate on her courses. Furthermore, I also would like to acknowledge Dr. Bo-Ting Liou. He is a very optimistic person and usually brings happiness into our laboratory. However, he is very serious regarding our research and always gives us great suggestions in weekly group meeting. I felt deeply honored that they can be my thesis committee members.

On the other hand, I would like to thank all of my dear friends, Yi-An Chang, Chih-Kang Chang, Sheng-Horng Yen, Yu-Hua Wu, Cheng-Yang Lin, Meng-Lun Tsai, Han-Yi Chu, Hsiu-Fen Chen, Shang-Wei Hsieh, Man-Lin Tu, Yung-Cheng Chang, Ming-Wei Yao, Bo-Jean Chen,

Cheng-Hong Yang, Chung-Hsien Lee, Syuan-Huei Horng, Chien-Fang Chiu, and other members in our laboratory.

Finally, I would like to sincerely acknowledge my family, mother, father, sisters, and brother. They always believed in me and encouraged me to do everything I wanted to do. I could not be here without them. I also would like to thank my dear girlfriend, Helen. She is an optimistic and considerate person. I am lucky to meet her in my life.

Table of Contents

List of Figures.......... V

List of Tables.......... IX

Abstract.......... X

Chapter 1. Introduction.......... 1

1.1 Introduction to VCSELs.......... 5

1.1.1 Structures.......... 9

1.1.2 Design of Bragg Reflectors.......... 15

1.1.3 Gain/Cavity Resonance Alignment.......... 22

1.1.4 MBE and MOVPE Growth Techniques.......... 25

1.2 Theoretical Considerations.......... 30

1.2.1 Band Structure: The $k{\cdot}p$ Method.......... 30

1.2.2 Optical Gain Model.......... 33

1.2.3 Strain Effects.......... 36

1.2.4 Critical Thickness for Strained Layer.......... 39

Chapter 2. Optimization Study of the InGaAlAs Quantum-Well Structures for 850-nm VCSELs.................................... 43

2.1 Study Related to the Compressively Strained 850-nm InGaAlAs VCSELs... 44

2.2 Physical Model and Parameters..................................... 46

2.3 Simulation Result and Discussion................................. 50

2.4 Summary.. 62

Chapter 3. Optimization Study of the InGaAsP Quantum-Well Structures for 850-nm VCSELs..................................... 63

3.1 Study Related to the Compressively Strained 850-nm InGaAsP VCSELs... 64

3.2 Physical Model and Parameters...................................... 66

3.3 Simulation Result and Discussion................................. 69

3.4 Summary.. 80

Chapter 4. Conclusion.. 81

Appendix A. Publication List... i

List of Figures

Fig. 1.1 The relation between bandgap energy (emission wavelength) and lattice constant for most important ternary and quaternary alloy families of interest for VCSELs……………………… 3

Fig. 1.2 Sketch of semiconductor laser diode structures. (a) VCSEL. (b) Edge emitting laser……………………………………… 6

Fig. 1.3 (a) The lasing mode of an edge-emitting laser changes with temperature evidently due to the alignment with the peak of gain spectrum. (b) The lasing mode of a VCSEL does not change with temperature distinctly due to the larger spacing between cavity modes…………………………………… 7

Fig. 1.4 Device structures used for transverse optical and/or electrical confinement. (a) Etched air-post, (b) ion-implanted, (c) regrown buried heterostructure, and (d) oxide-confined VCSELs…... 11

Fig. 1.5 (a) Oxidation rate at 420 °C for 100-nm-thick $Al_xGa_{1-x}As$ layers with x varying from 0.84 to 1.0 surrounded by 100-nm-thick GaAs layers. (b) Oxidation rate of 84-nm-thick $Al_xGa_{1-x}As$ versus temperature for x = 1.0, 0.98, and 0.92. (c) AlAs oxidation rate at 400 °C versus AlAs layer thickness……… 13

Fig. 1.6 A plane wave with TE polarization is incident on a multilayered medium………………………………………………... 16

Fig. 1.7 Reflection spectra and phase change on reflection of (a) 5-pairs, (b) 15-pairs, and (c) 40-pairs $Al_{0.15}Ga_{0.85}As/Al_{0.9}Ga_{0.1}As$ DBR designed at 850 nm………………………………………. 19

Fig. 1.8 (a) Reflection spectra of 40-pairs $Al_{0.15}Ga_{0.85}As/Al_{0.9}Ga_{0.1}As$

DBR with the incident angles of 0 and 10 degree. (b) Reflectivity of 5-, 15-, and 40-pairs $Al_{0.15}Ga_{0.85}As/Al_{0.9}Ga_{0.1}As$ DBR at 850 nm for various incident angle………………… 20

Fig. 1.9 Schematic representation of the relation between conduction band edge energy and longitudinal optical field for a general QW VCSEL structure……………………………………… 21

Fig. 1.10 (a) Schematic representation of the spectral alignment between the cavity mode and the gain spectrum in a VCSEL. (b) Variations in VCSEL threshold current caused due to the different thicknesses of the cavity across a wafer. (c) Variations in VCSEL threshold current for a given VCSEL as a function of substrate temperature………………………………………. 23

Fig. 1.11 Schematic diagram of MBE growth reactor……………….. 26

Fig. 1.12 Schematic illustration of a MOVPE system……………….. 29

Fig. 1.13 Crystal lattice deformation under compressive strain. The z axis represents the quantum-well growth direction…………….. 36

Fig. 1.14 The valence subband structure of an 80 Å $GaAs/Al_{0.2}Ga_{0.8}As$ quantum well and the total (solid curve) and H1 subband (dashed curve) density of states plotted relative to the density of states in the first conduction (C1) subband……………….... 37

Fig. 1.15 The valence subband structure of an 80 Å $In_{0.2}Ga_{0.8}As/Al_{0.2}Ga_{0.8}As$ quantum well and the total (solid curve) and H1 subband (dashed curve) density of states plotted relative to the density of states in the first conduction (C1) subband.. 38

Fig. 1.16 The critical thickness of $In_xGa_{1-x}As/GaAs$ as a function of indium composition calculated by the Matthews and Blakeslee model for (a) superlattice, (b) quantum well, and (c) single

strained layer structures…………………………………… 40

Fig. 1.17 Comparison of the calculated critical thicknesses for $In_xGa_{1-x}As/GaAs$ single layers as a function of indium composition according to the Matthews and Blakeslee model and the People and Bean model…………………………… 41

Fig. 2.1 The valence subband structures for 7-nm InGaAlAs quantum well sandwiched between $Al_{0.3}Ga_{0.7}As$ barriers for (a) $In_{0.02}Ga_{0.98}As$, (b) $In_{0.08}Ga_{0.883}Al_{0.037}As$, (c) $In_{0.14}Ga_{0.786}Al_{0.074}As$, (d) $In_{0.20}Ga_{0.671}Al_{0.119}As$, and (e) $In_{0.26}Ga_{0.585}Al_{0.155}As$…….. 52

Fig. 2.2 Room-temperature (a) TE and (b) TM gain spectra for compressively strained 7-nm $In_{0.02}Ga_{0.98}As$ and InGaAlAs quantum wells with $Al_{0.3}Ga_{0.7}As$ barrier. The input carrier concentration is 6×10^{18} cm^{-3}……………………………… 54

Fig. 2.3 Gain peak of TE mode as a function of carrier density for $In_{0.02}Ga_{0.98}As$ and variant InGaAlAs quantum wells with $Al_{0.3}Ga_{0.7}As$ barrier at (a) 25 °C and (b) 95 °C…………… 55

Fig. 2.4 Gain peak of TE mode as a function of radiative current density for $In_{0.02}Ga_{0.98}As$ and variant InGaAlAs quantum wells with $Al_{0.3}Ga_{0.7}As$ barrier at (a) 25 °C and (b) 95 °C…………… 56

Fig. 2.5 (a) Transparency carrier density and (b) transparency radiative current density of TE mode as a function of compressive strain at 25 °C and 95 °C………………………………………… 58

Fig. 2.6 Maximum differential gain of TE mode as a function of compressive strain at 25 °C and 95 °C……………………. 59

Fig. 3.1 Valence subband structures for 8-nm InGaAsP quantum well sandwiched between $In_{0.4}Ga_{0.6}P$ barriers for (a) $In_{0.02}Ga_{0.98}As_{0.981}P_{0.019}$, (b) $In_{0.12}Ga_{0.88}As_{0.892}P_{0.108}$, (c)

$In_{0.22}Ga_{0.78}As_{0.799}P_{0.201}$, (d) $In_{0.32}Ga_{0.68}As_{0.704}P_{0.296}$, and (e) $In_{0.42}Ga_{0.58}As_{0.607}P_{0.393}$……………………………………….. 70

Fig. 3.2 Gain spectra of compressively strained InGaAsP/InGaP quantum wells at (a) 25 °C and (b) 95 °C………………… 72

Fig. 3.3 Peak material gain of TE mode as a function of carrier density for InGaAsP/InGaP quantum wells at (a) 25 °C and (b) 95 °C……………………………………………………. 74

Fig. 3.4 Peak material gain of TE mode as a function of radiative current density for InGaAsP/InGaP quantum wells at (a) 25 °C and (b) 95 °C…………………………………………………… 75

Fig. 3.5 (a) Transparency carrier density and (b) transparency radiative current density of TE mode as a function of compressive strain at 25 °C and 95 °C……………………………………... 76

Fig. 3.6 Maximum differential gain of TE mode as a function of compressive strain at 25 °C and 95 °C…………………… 77

List of Tables

Table 2.1 Parameters of the binary semiconductors GaAs, AlAs, and InAs………………………………………………………… 47

Table 2.2 Varshni parameters of the binary semiconductors GaAs, AlAs, and InAs………………………………………………………. 49

Table 2.3 Calculated critical thicknesses of InGaAs and InGaAlAs quantum wells with Matthews and Blakeslee model……. 60

Table 3.1 Material parameters of the binary semiconductors GaAs, InAs, GaP and InP……………………………………………... 68

Table 3.2 Varshni parameters of the binary semiconductors GaAs, InAs, and InP…………………………………………………... 68

Table 3.3 Calculated critical thicknesses of InGaAsP quantum wells with Matthews and Blakeslee model……………………. 78

中文摘要

本文利用 6×6 Luttinger-Kohn Hamiltonian 理論探討可用於 850-nm 面射型雷射之壓縮應力砷化鋁鎵銦與砷磷化銦鎵量子井結構。一般而言，大部份 850-nm 面射型雷射均以晶格匹配的砷化鎵量子井做為活性層材料，然而應用壓縮應力以降低雷射臨界電流和提高調變速率的方法已被廣泛使用於量子井雷射。因此本文將研究具有不同壓縮應力之砷化銦鎵、砷化鋁鎵銦與砷磷化銦鎵量子井結構，進而探討最佳的壓縮應力值。在文章一開始，首先對於面射型雷射的發展與設計原理做一簡短描述，其次將針對本文數值模擬相關的理論模型與物理參數做一簡介與總整。

本文主體首先研究不同壓縮應力砷化鋁鎵銦量子井之特性，其中包含價電帶能帶結構、增益頻譜、透明載子濃度及透明輻射電流密度。模擬結果顯示，砷化鋁鎵銦量子井之最大增益值、透明載子濃度、透明輻射電流密度與微分增益將隨著量子井壓縮應力的增加而獲得改善。然而，當壓縮應力值約大於 1.5%時，砷化鋁鎵銦量子井材料特性的改善將有接近於飽和的現象，此結果可由價電帶能帶結構隨著壓縮應力的變化而得到解釋。除此之外，本文亦以相似的研究方法探討不同壓縮應力之砷磷化銦鎵量子井結構，由模擬結果得知，雖然光學增益、透明載子濃度、透明輻射電流密度與微分增益可藉由增加砷磷化

銦鎵量子井之壓縮應力而得到改善，但是當壓縮應力值約高於 1.24%時，其改善的現象已不明顯。

雖然利用較高壓縮應力之量子井可以使砷化鋁鎵銦與砷磷化銦鎵量子井的相關特性獲得改善，然而以實際長晶的觀點而言，具有較高應力的量子井可能影響晶體品質。因此，根據模擬結果，砷化鋁鎵銦與砷磷化銦鎵量子井結構的最佳壓縮應力值分別為 1.5%和 1.24%。

Abstract

In this thesis, numerical simulation based on 6×6 Luttinger-Kohn Hamiltonian is utilized to investigate the optical gain and threshold properties of compressively strained InGaAlAs/AlGaAs and InGaAsP/InGaP quantum-well structures grown on GaAs substrate for 850-nm vertical-cavity surface-emitting lasers. Most 850-nm VCSEL devices usually utilize an unstrained GaAs/AlGaAs quantum-well structure. However, lower threshold current and higher modulation speed can be achieved by employing compressive strain in quantum-well lasers. For this reason, alternative material systems including InGaAs, InGaAlAs, and InGaAsP with different compressive strains are explored in an attempt to obtain optimal strain level. In this thesis, first of all, the development and the design considerations of vertical-cavity surface-emitting lasers are briefly described. Next, the theoretical models and physical parameters employed in this work are introduced and summarized.

For the main portion of this thesis, the valence subband structures, optical gain spectra, transparency carrier densities, and transparency radiative current densities of different compressively strained InGaAlAs quantum wells with $Al_{0.3}Ga_{0.7}As$ barriers are systematically investigated. Numerical simulation results suggest that the maximum optical gain, transparency carrier densities, transparency radiative current densities, and differential gain of InGaAlAs quantum wells can be enhanced by introducing more compressive strain in

quantum wells. However, further improvement of the optical properties of InGaAlAs quantum wells becomes minimal when the compressive strain is higher than approximately 1.5%. This result is mainly attributed to the valence subband structures which vary with the compressive strain in the quantum wells. Moreover, different compressively strained InGaAsP quantum wells with $In_{0.4}Ga_{0.6}P$ barriers are also discussed by using similar research method. The results of numerical calculations show that while the maximum optical gain, transparency carrier densities, transparency radiative current densities, and differential gain of InGaAsP quantum wells can be improved with increasing compressive strain in quantum wells, further improvement of the optical gain and threshold properties of the InGaAsP quantum-well structures becomes minimal when the compressive strain in quantum wells is higher than approximately 1.24%.

Although the properties of compressively strained InGaAlAs and InGaAsP quantum wells can be improved by employing larger amount of compressive strain in quantum wells, from the viewpoint of epitaxial growth, a higher level of strain in quantum wells may have crystal quality concerns. Therefore, according to the simulation results, the optimal compressive strains for InGaAlAs/AlGaAs and InGaAsP/InGaP quantum wells are approximately 1.5% and 1.24%, respectively.

Chapter 1. Introduction

Nowadays, optoelectronic devices have become an important part of our lives. These include photodiodes, solar cells, light-emitting diodes (LEDs), laser diodes (LDs) and so on. Photodiodes convert a light signal to an electrical signal such as a voltage or current. Solar cells have received great attention in recent years since they can convert the incident sunlight into a useful form of energy. LEDs have been widely used to replace the traditional traffic lights to reduce power consumption. White LEDs may become the mainstream lighting technology in homes, offices, and public places in the future. LDs are used in the applications from the writing or readout sources in compact disk players to the light sources in optical fiber communication systems. Because various applications can be achieved by using these optoelectronic devices, research on this field has been advanced rapidly.

Most optoelectronic devices are typically made from III-V compound semiconductors due to their direct bandgap characteristics. Furthermore, one of the most important factors for using III-V compound semiconductors is that the heterostructure devices can be constructed from binary, ternary, and quaternary alloys. Thus, electrons and holes are confined to dimensions on the order of a nanometer to enhance the recombination rate. Besides, by varying the elements and compositions of ternary and quaternary alloys, the emission wavelengths of LEDs and LDs can cover a spectral range from

ultraviolet to infrared. Figure 1.1 shows the relation between bandgap energy (emission wavelength) and lattice constant for the most important ternary and quaternary alloy families of interest for VCSELs [1]. This figure is significant for the design of most optoelectronic devices. Lattice constant is an important parameter for epitaxial growth. This is primarily because the crystal quality depends on the degree of lattice matching. Energy gap dominates the emission or absorption wavelength for optoelectronic devices. Therefore, it is important that the lattice constant and energy bandgap can be read from this figure simultaneously. However, for light-emitting devices, we should notice that the materials of an emitting layer are direct or indirect bandgap semiconductors. The majority of light-emitting devices are fabricated with direct bandgap semiconductors in which electron-hole pairs can recombine directly and release their energy in the form of light. On the contrary, the recombination process in indirect bandgap materials requires the help of phonon absorption or phonon emission, which will reduce the conversion efficiency for light-emitting devices. Thus, several indirect bandgap materials such as silicon (Si), germanium (Ge), aluminum arsenide (AlAs), gallium phosphide (GaP), and aluminum phosphide (AlP) are not suitable for light-emitting devices. However, nitrogen doped indirect bandgap GaP or GaAsP alloys are widely used in green, yellow, and orange LEDs due to the limit of epitaxy technology and the lack of suitable direct bandgap materials in the early development. Although several indirect bandgap materials can be taken as

an emitting layer of LEDs, it is nearly impossible that the indirect bandgap materials are used to be an emitting layer of high-performance LDs.

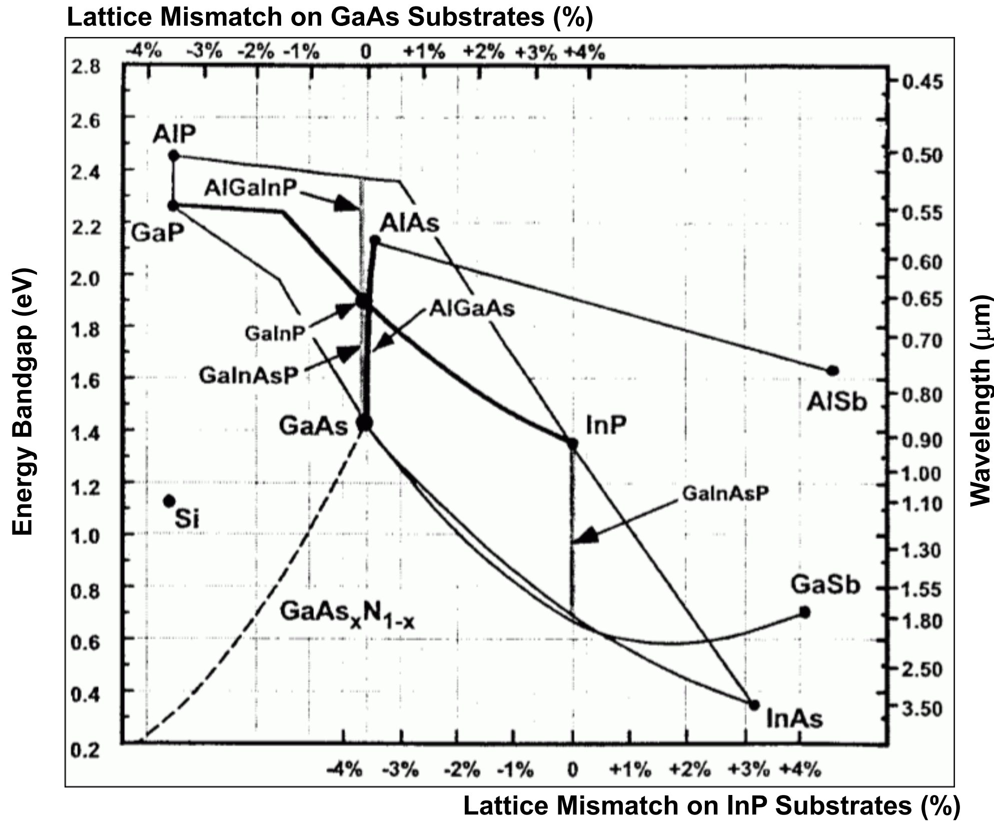

Fig. 1.1. The relation between bandgap energy (emission wavelength) and lattice constant for most important ternary and quaternary alloy families of interest for VCSELs. (After Ref. 1)

LDs are preferred, as compared with conventional gas or solid-state lasers, due to their small size, low cost, and ease of operation using low voltage power supplies. These properties are unique to make LDs as an ideal laser pick-up head for the optical data storage systems, such as Digital Versatile Disk (DVD) players. As for the development of LDs, laser emission was successfully demonstrated in semiconductor p-n junctions by

a number of laboratories in 1962 [2–5]. After that, the laser structures were improved by using cleaved laser mirror and double heterostructure (DH) [6]. A double heterostructure laser consists of an active layer embedded in two higher bandgap cladding layers. Thus, it confines the electrons and holes in the active layer to increase the recombination rate. Fortunately, when the energy band gap decreases, the index of refraction increases for most semiconductor materials. In this condition, a cladding layer has a lower index of refraction than that of an active layer, which forms an optical waveguide. Therefore, a DH laser confines the carriers and photons in the same range simultaneously, which enhances the rate of stimulated emissions. When the active layer is thinner than about 10 nm, the electrons are confined to a small region of space, and that produces discrete energy levels, instead of a continuum, according to quantum theory. Under this condition, the density of states in conduction and valence band are reduced, which makes the threshold current for population inversion markedly reduced as compared with DH lasers. The idea of employing quantum effect in LDs was generated in the early 1970s. After that, semiconductor lasers such as LDs, vertical-cavity surface-emitting lasers (VCSELs), and distributed feedback (DFB) lasers have utilized the quantum-well (QW) structures in the active region until now.

After the introduction of III-V compound semiconductors and semiconductor lasers, in the following subsections, I would like to focus on the laser structures and the design of VCSELs.

1.1 Introduction to VCSELs

Vertical-cavity surface-emitting lasers are relatively modern laser light sources as compared with LDs. The first VCSEL with an emission wavelength at 1180 nm was demonstrated by Soda *et al.* in 1979, in which the InGaAsP/InP material system was used as the active region [7]. This device incorporated metallic reflectors and a large active volume. Thus, the threshold current density was 44 kA/cm^2 at 77 K. To reduce the threshold current, a small active volume and high reflectivity mirrors are required. However, metallic reflectors are limited in reflectivity to about 98% because of the optical absorption. Another more suitable laser mirror for VCSELs is a distributed Bragg reflector (DBR), which can provide a reflectivity of higher than 99.99%. The first VCSEL which used such reflectors was shown by Ogura *et al.* in 1987 [8]. Since the active volume in this device was still large, the threshold current density was 1 kA/cm^2 at room temperature. The threshold current densities of VCSELs did not reduce obviously until Lee *et al.* employed the very high reflectivity mirrors (R~99.9%) and very small active volume (10-nm $In_{0.2}Ga_{0.8}As$ single QW) within device structure in 1989 [9]. The threshold current density of continuous-wave (CW) operation was reduced to 1.8 kA/cm^2 at room temperature. After that, many laboratories devoted their resources to developing VCSEL technology. To date, VCSELs have become a useful device for several applications, such as free space optical interconnects and

fiber-optic communications. Other VCSEL applications under development include compact disc optical pickup modules, printing heads, optical scanners, optical displays, projection systems, and optical sensors.

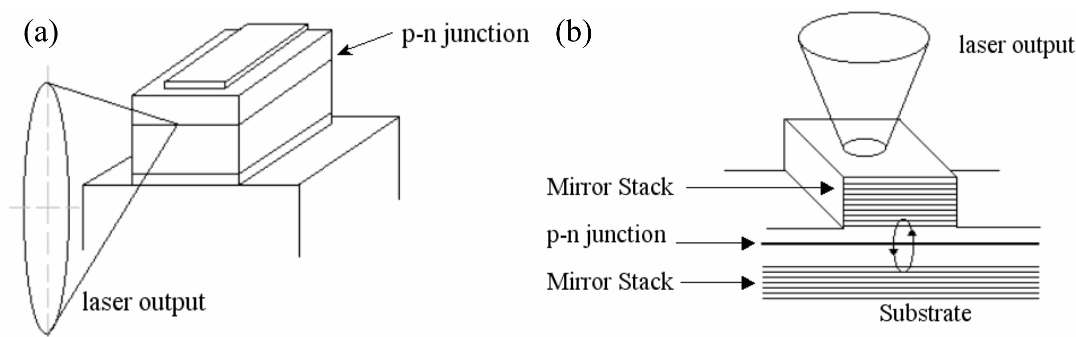

Fig. 1.2. Sketch of semiconductor laser diode structures. (a) VCSEL. (b) Edge emitting laser.

From the structural point of view, the VCSEL is substantially different from conventional LDs. The conventional LD is often referred to as an edge-emitting laser, as shown in Fig. 1.2 (a). Since the optical confinement is different in vertical and transverse directions, the far-field pattern of the laser beam is elliptic, which makes the laser beam coupled into optical fiber difficult. On the contrary, the VCSEL circumvents the problems caused from edge emission by having its optical cavity in the vertical direction, as shown in Fig. 1.2 (b). In this situation, the VCSEL can provide a low divergence circular laser beam as an ideal light source for optical communications. On the other hand, as compared with edge-emitting lasers, VCSELs offer many advantages in fabrication and test. This is mainly due to the fact that the on-wafer testing before packaging will enable

high-volume and low-cost manufacturing. Unlike a VCSEL, laser mirrors of an edge-emitting laser are fabricated by cleaving or etching. Besides, after completing many processes, such as facet passivation, coating, and packaging, optical testing of the laser chip can be performed. It is time-consuming and costly to finish these processes for edge-emitting lasers.

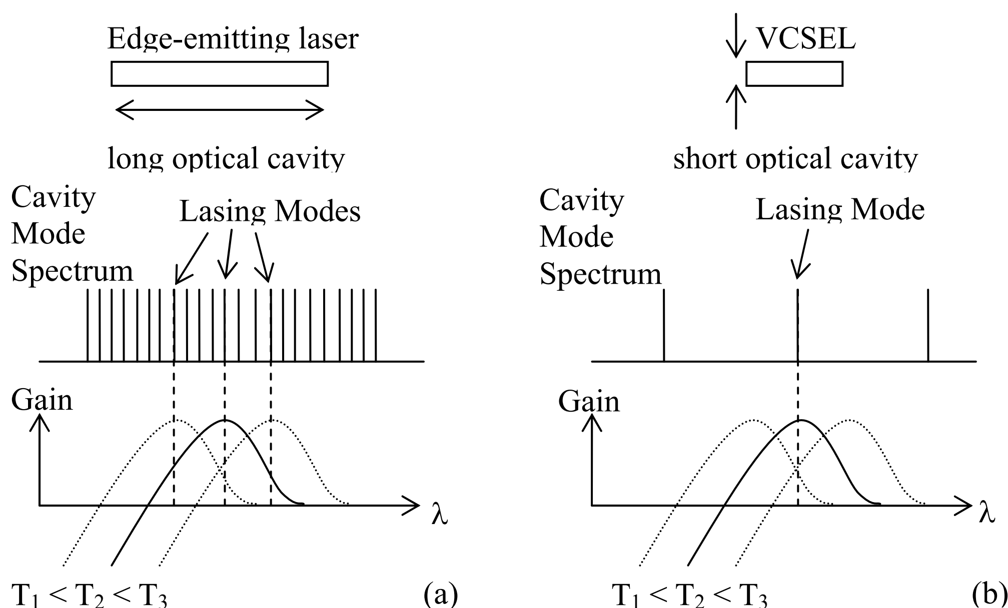

Fig. 1.3. (a) The lasing mode of an edge-emitting laser changes with temperature evidently due to the alignment with the peak of gain spectrum. (b) The lasing mode of a VCSEL does not change with temperature distinctly due to the larger spacing between cavity modes.

Moreover, another important distinction is the short cavity length of the VCSEL compared to a typical edge-emitting laser. As shown in Fig. 1.3 (a), the mode separation of a regular edge-emitting laser is so small that the

lasing mode is always near the peak of the gain spectrum. As the device temperature increases with the injection current, the lasing mode shifts to longer wavelengths with the gain spectrum obviously. It means that the emission wavelength is sensitive to device temperature. However, as for a VCSEL, if we design the cavity length on the order of a few wavelengths, it is possible to only have single longitudinal mode in the range of gain spectrum, as shown in Fig. 1.3 (b). Under this circumstance, although the gain spectrum of the active region changes with temperature, the lasing mode is dependent on where the cavity mode falls on the gain spectrum. Thus, the emission wavelength is relatively insensitive to device temperature, which is very important for a VCSEL to be a light source in an optical communication system.

In addition to these advantages, the small active volume of a VCSEL reveals that the threshold current can be smaller than 1 mA. This feature is critical in low-power lasers for the requirements of high modulation speed and high efficiency. Response speed is increased by operating a diode laser with currents above the threshold current. Thus, the amount of input current required consistent with a given speed can be reduced by lowing laser thresholds. For the applications of low-power lasers, 1 mW of optical power is usually ample. Other requirements such as low-current operation, high modulation speed, and high efficiency appear to be better met by VCSELs than by edge-emitting lasers.

Because of the differences in laser structures, the inherent advantages

in VCSELs make some characteristics comparable to or better than those of edge-emitting lasers. However, there are still many difficulties associated with the development of high power, single mode, and GaN-based VCSELs. These are the specific targets of continuing research and development efforts about VCSELs in the future.

1.1.1 Structures

The structure of a VCSEL generally consists of *p*-type DBR, *n*-type DBR, and optical cavity. The DBR mirrors provide longitudinal optical confinement. Nevertheless, it is also important for finding ways to confine the electrical current and optical mode effectively in the lateral extent of the laser cavity. As indicated in Fig. 1.4, there are four basic device structures: the etched air-post, ion implanted, regrown buried heterostructure, and oxide-confined VCSEL structures. The characteristics of these structures will be reviewed briefly in this subsection. However, the oxide-confined VCSEL structure is emphasized and further discussed at the end of this subsection since it presently provides the most effective confinement of both carriers and photons.

First of all, the simplest method to form the transverse optical and electrical confinement is to etch a pillar or post, as shown in Fig. 1.4 (a). This process has to be achieved by means of chemically assisted ion beam etching or reactive ion etching due to the requirement of small cross-section

areas and smooth vertical side walls [10–13]. Since the index difference between air and the etched semiconductor is large, strong index guiding is present in the lateral direction. In this condition, VCSELs typically exhibit multiple transverse modes above lasing threshold [14]. Besides, the air-post VCSEL causes carrier loss due to surface recombination at the side walls, which is induced by the defective etched surface. Optical loss with greater etch depth and high thermal resistance are also the important considerations about air-post VCSELs.

Secondly, as depicted in Fig. 1.4 (b), the ion implantation technique can also be used to define the lateral active region. This mechanism is that the top DBR where is implanted by certain high energy species, such as protons or oxygen ions, will become insulating due to the crystalline damage. Accordingly, the flow of the injection current can be confined in a small area of the active layer. However, it is important to prevent the possibility of active region damage in implanted VCSELs since defects in active region will cause significant optical and carrier losses. Although the current path can be defined by ion implantation technique, inherent transverse optical confinement does not exist in this structure. Transverse modes are supported by a thermally induced refractive index gradient, which is called the thermal lensing effect [15, 16]. Under this circumstance, implanted VCSELs still have multilateral-mode behavior owing to the spatial hole burning effect [17].

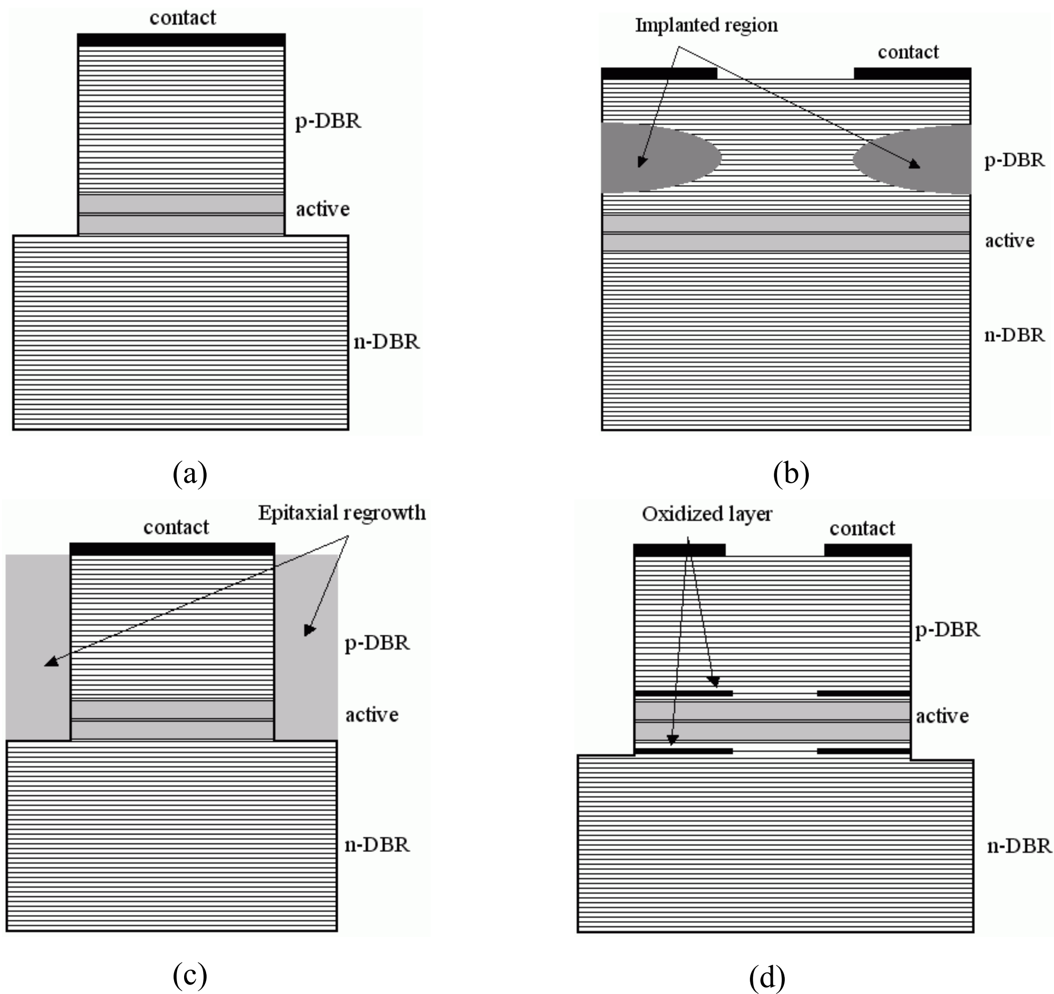

Fig. 1.4. Device structures used for transverse optical and/or electrical confinement. (a) Etched air-post, (b) ion-implanted, (c) regrown buried heterostructure, and (d) oxide-confined VCSELs.

Next, as compared with air-post VCSELs, an approach that prevents the strong index guiding and the difficult thermal dissipation involves using a buried heterostructure, as shown in Fig. 1.4 (c). This structure is processed by etching away the materials around the intended cavity. Then, the etched regions are replaced with higher bandgap and lower index

materials. By this technique, index guiding and electrical confinement are achieved simultaneously. However, fabricating the regrown buried heterostructure VCSELs is particularly challenging since it requires growth on high Al content AlGaAs surfaces. The native oxides that form on AlGaAs surfaces cannot be removed easily. Therefore, special etching techniques and avoidance of air exposure are important for epitaxial regrowth.

As for the fourth structure, it is relatively straightforward to utilize the selective oxidation to provide index guiding and electrical confinement simultaneously, as illustrated in Fig. 1.4 (d). Since the oxide layer is formed by converting the Al-rich AlGaAs layer to a robust insulating oxide, the oxide layer can be designed at different locations in DBR stacks. Fortunately, the oxidation rate of $Al_xGa_{1-x}As$ for x varying from 0.84 to 1.0 is extremely sensitive to Al composition, as shown in Fig. 1.5 (a) [18, 19]. It is achievable to discriminate the oxidation rates between the high Al-content layer and the DBR by this oxidation selectivity. On the other hand, the oxidation temperature and the thickness of the AlGaAs layer are also critical process parameters. Fig. 1.5 (b) shows the oxidation rates of $Al_xGa_{1-x}As$ versus temperature for x = 1.0, 0.98, and 0.92, respectively [19]. By comparing the oxidation rates of $Al_{0.98}Ga_{0.02}As$ and $Al_{0.92}Ga_{0.08}As$, it is obvious that the difference of oxidation rates increases with temperature from 380 °C to 500 °C. Figure 1.5 (c) illustrates the oxidation rate of AlAs layers of varying thickness [19]. It is noteworthy that the oxidation rate is

nearly constant when the layer thickness is larger than about 60 nm. In conclusion, to decide the oxide aperture size precisely, stringent control of Al composition and thickness of the AlGaAs layer as well as the oxidation temperature is necessary.

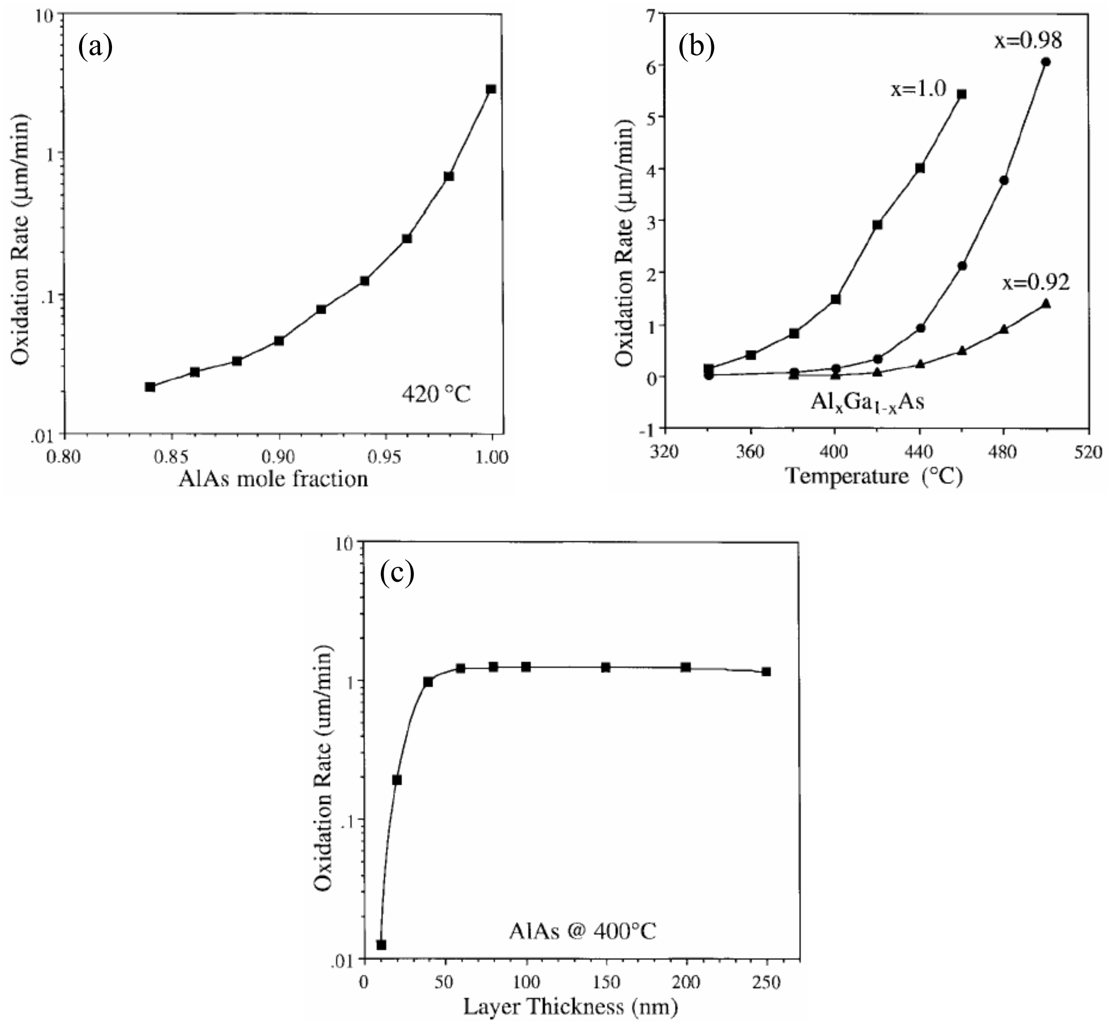

Fig. 1.5. (a) Oxidation rate at 420 °C for 100-nm-thick $Al_xGa_{1-x}As$ layers with x varying from 0.84 to 1.0 surrounded by 100-nm-thick GaAs layers. (b) Oxidation rate of 84-nm-thick $Al_xGa_{1-x}As$ versus temperature for x = 1.0, 0.98, and 0.92. (c) AlAs oxidation rate at 400 °C versus AlAs layer thickness. (After Ref. 19)

Although the transverse confinement can be carried out by the oxide layer due to the significantly lower refractive index than the original semiconductor layer, the laser performance depends greatly on the thickness of the oxide layer, the position of the oxide layer, and the oxide aperture. The thickness of the oxide layer can be used to control the induced effective index difference between the cavity and the surrounding region including the oxide layer [20]. As for the position of the oxide layer, Bond *et al.* have studied the effects of the oxide layer placed at a node and at a peak in the standing wave on the properties of VCSELs. They found that the optical loss appeared to be negligible when the oxide layer was placed at a node [21, 22]. On the contrary, the threshold current increased as the oxide layer was placed at the peak of the optical standing wave. It is attributed to the enhanced optical loss as the oxide layer is placed at an antinode. Furthermore, the dependence of the oxide aperture size on the laser performances is a trade-off. In general, the threshold current decreases with smaller oxide aperture. However, the maximum output power will decrease with smaller oxide aperture due to the dramatic increase of the thermal resistance [23, 24]. Since most VCSEL properties, such as threshold current, maximum output power, threshold voltage, far-field pattern, modulation speed, and mode spectrum are dependent on the design of the oxide layer, the optimization study of the oxide layer for VCSELs is still under study.

1.1.2 Design of Bragg Reflectors

Since VCSELs utilize DBRs as the laser mirrors to achieve high reflectivity, an appropriate and accurate DBR design is a significant consideration for VCSEL devices. The DBR mirrors consist of alternating pairs of quarter-wavelength thick high and low refractive index layers. Although the dielectric materials are also used to form the DBR mirrors due to the advantage of large refractive index difference, most VCSEL devices still employ the semiconductor materials in DBR mirrors, which simplifies the VCSEL fabrication and allows current injection through the mirrors into the active medium.

Semiconductor DBR mirrors typically have lower index contrast and thus require a greater number of periods for high reflectivity. From the epitaxy point of view, fortunately, the GaAs lattice constant is approximately the same as AlAs, as shown in Fig. 1.1. It is the main reason why the AlGaAs material system is widely used in DBR mirrors. The aluminum compositions of the AlGaAs materials in DBR stack are chosen in an attempt to maximize their index contrast. However, it should be noticed that each DBR layer must be transparent to the laser emission. Besides, in the case of material systems that lack high index contrast and lattice-matched alloys such as InGaAsP/InP system, wafer-bonding technology can be used to fuse DBR mirrors and active regions even if the lattice constants of these materials are different [25].

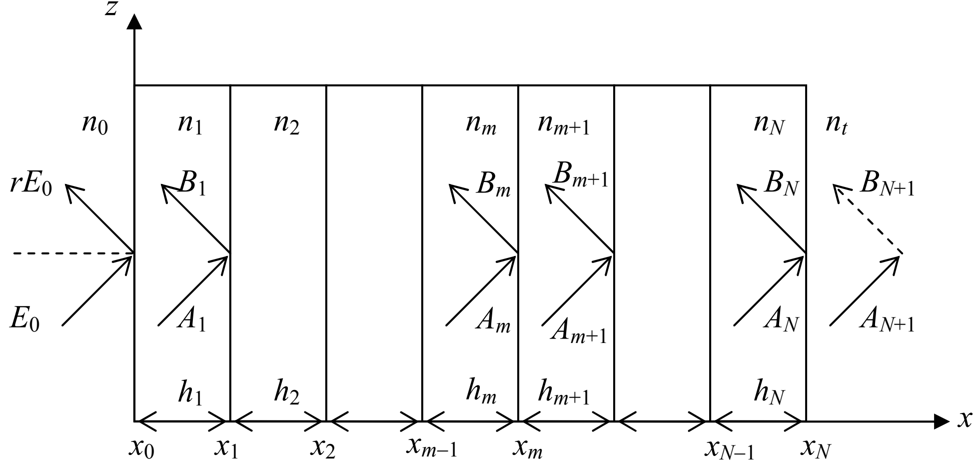

Fig. 1.6. A plane wave with TE polarization is incident on a multilayered medium.

In order to estimate the reflectivity and mirror stopband of a certain DBR mirror, numerical calculation of multilayered mirrors is necessary. Transfer matrix method is generally used to calculate the reflection spectra of multilayered mirrors with abrupt interfaces [26]. As shown in Fig. 1.6, for a TE polarized incident wave

$$\vec{E}_i = \hat{y}E_0 \mathrm{e}^{ik_{0x}x+ik_{0z}z}, \tag{1.1.1}$$

and, for the reflected wave, the electric field can be expressed as

$$\vec{E}_r = \hat{y}rE_0 \mathrm{e}^{-ik_{0x}x+ik_{0z}z}. \tag{1.1.2}$$

In the mth layer, $x_{m-1} \le x \le x_m$, the electric field and magnetic field are given by $\vec{E}_m = \hat{y}E_y^m$,

$$E_y^m = \left(A_m \mathrm{e}^{ik_{mx}(x-x_m)} + B_m e^{-ik_{mx}(x-x_m)}\right)e^{ik_{mz}z}, \tag{1.1.3}$$

$$H_z^m = \frac{k_{mx}}{\omega\mu_0}\left(A_m \mathrm{e}^{ik_{mx}(x-x_m)} - B_m e^{-ik_{mx}(x-x_m)}\right)e^{ik_{mz}z}, \tag{1.1.4}$$

where $k_{mz} = k_{0z}$ for all m,

$$k_{mx} = \frac{2\pi\, n_m}{\lambda}\cos\theta + i\alpha_m. \tag{1.1.5}$$

α_m is the scattering and absorption loss in the mth layer. Employing the boundary conditions at $x = x_m$, we have

$$\begin{bmatrix} A_m \\ B_m \end{bmatrix} = M_{m(m+1)} \begin{bmatrix} A_{m+1} \\ B_{m+1} \end{bmatrix}, \tag{1.1.6}$$

where

$$M_{m(m+1)} = \frac{1}{2}\begin{bmatrix} (1+P_{m(m+1)})\mathrm{e}^{-ik_{(m+1)x}h_{m+1}} & (1-P_{m(m+1)})\mathrm{e}^{ik_{(m+1)x}h_{m+1}} \\ (1-P_{m(m+1)})\mathrm{e}^{-ik_{(m+1)x}h_{m+1}} & (1+P_{m(m+1)})\mathrm{e}^{ik_{(m+1)x}h_{m+1}} \end{bmatrix}. \tag{1.1.7}$$

We have defined $h_{m+1} = x_{m+1} - x_m$ and

$$P_{m(m+1)} = \frac{k_{(m+1)x}}{k_{mx}}. \tag{1.1.8}$$

The amplitudes of the incident and reflected waves are related to those amplitudes in the transmitted region N+1 by

$$\begin{bmatrix} E_0 \\ rE_0 \end{bmatrix} = M_{01}M_{12}M_{23}\cdots M_{N(N+1)} \begin{bmatrix} A_{N+1} \\ B_{N+1} \end{bmatrix}$$

$$= \begin{bmatrix} m_{11} & m_{12} \\ m_{21} & m_{22} \end{bmatrix} \begin{bmatrix} tE_0 \\ 0 \end{bmatrix}, \tag{1.1.9}$$

where $B_{N+1} = 0$, since there is no incident wave in this region, as illustrated in Fig. 1.6. We can obtain the reflection coefficient of the multilayered medium by

$$r = \frac{m_{21}}{m_{11}}. \tag{1.1.10}$$

On the other hand, the transmission coefficient of the multilayered medium can be expressed by

$$t = \frac{1}{m_{11}}. \tag{1.1.11}$$

Therefore, the power reflectivity of the multilayered medium can be found by using

$$R = |r|^2. \tag{1.1.12}$$

Based on the transfer matrix method, the reflection spectra and phase change on reflection of (a) 5-pairs, (b) 15-pairs, and (c) 40-pairs $Al_{0.15}Ga_{0.85}As/Al_{0.9}Ga_{0.1}As$ DBR are plotted in Fig. 1.7. This DBR material system is widely used in 850-nm VCSELs. From Fig. 1.7, it is observed that the reflectivity increases with the number of DBR pairs. However, the width of the mirror stopband reduces as the number of DBR pairs increases. The reflectivity and the width of the mirror stopband are proportional to the refractive index difference between the high and low index layers in the DBR mirrors.

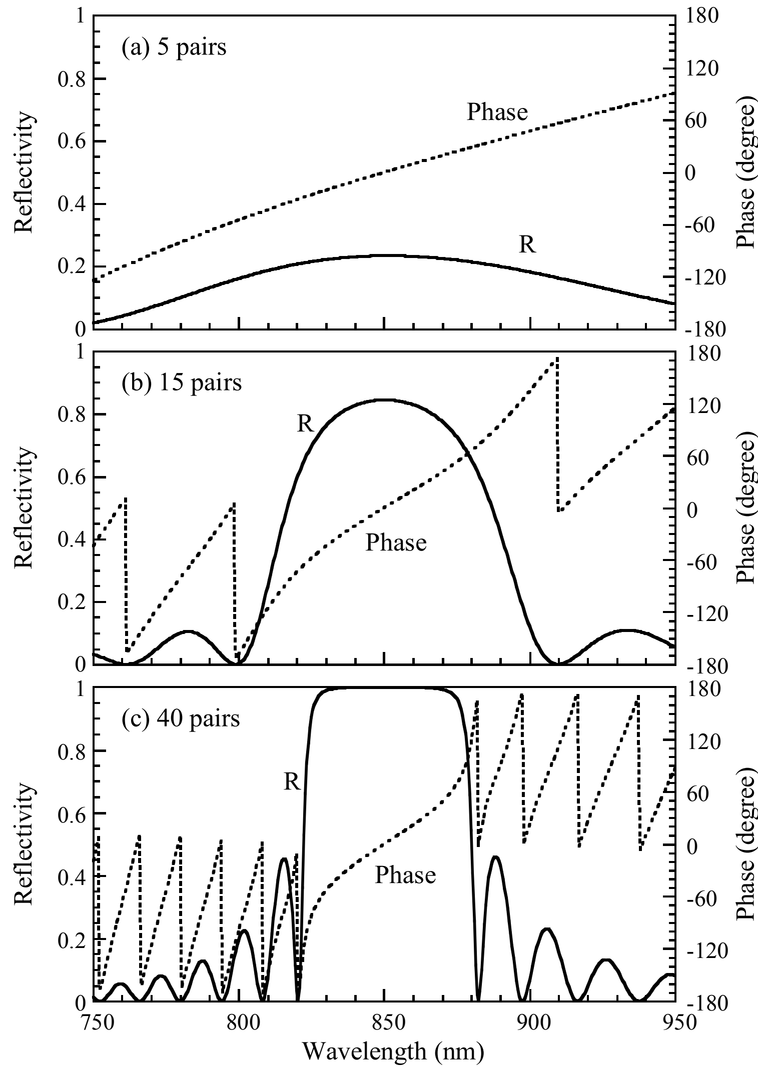

Fig. 1.7. Reflection spectra and phase change on reflection of (a) 5-pairs, (b) 15-pairs, and (c) 40-pairs $Al_{0.15}Ga_{0.85}As/Al_{0.9}Ga_{0.1}As$ DBR designed at 850 nm.

Figure 1.8 (a) shows the reflection spectra of the 40-pairs $Al_{0.15}Ga_{0.85}As/Al_{0.9}Ga_{0.1}As$ DBR with the incident angles of 0 and 10 degree. It is found that the incident light with an incident angle of 10 degree blue-shifts the reflection spectrum. Since DBR mirrors also can be used in resonant cavity LEDs (RCLEDs) [27], it is important for RCLEDs that the

reflectivity at specific wavelength changes with various incident angles. Figure 1.8 (b) shows the reflectivity of 5-, 15-, and 40-pairs $Al_{0.15}Ga_{0.85}As/Al_{0.9}Ga_{0.1}As$ DBR at 850 nm as a function of the incident angle. It can be seen that the angular stopband becomes narrower when the number of DBR pairs increases.

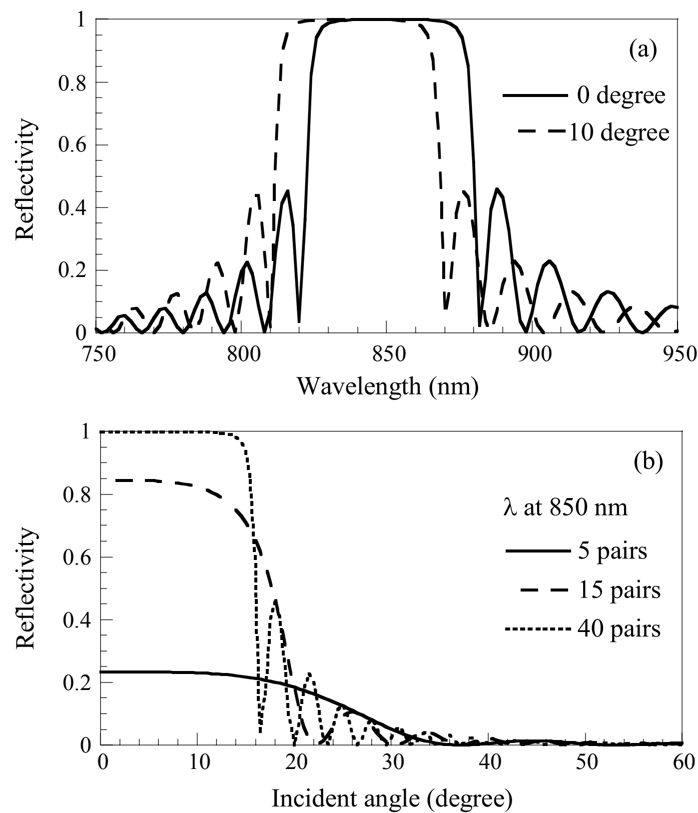

Fig. 1.8. (a) Reflection spectra of 40-pairs $Al_{0.15}Ga_{0.85}As/Al_{0.9}Ga_{0.1}As$ DBR with the incident angles of 0 and 10 degree. (b) Reflectivity of 5-, 15-, and 40-pairs $Al_{0.15}Ga_{0.85}As/Al_{0.9}Ga_{0.1}As$ DBR at 850 nm for various incident angle.

While the large index contrast provided by heterojunctions is necessary to achieve high DBR reflectivity, it also implies that large energy band offsets will impede current transport through the semiconductor DBR and

result in high series resistance [28]. This problem must be considered particularly in *p*-type DBR because the large hole mass lowers the probability of tunneling and thermionic emission. Although the resistance can be reduced by increasing doping concentration in DBR layers, higher doping concentration also increases optical absorption due to the light transport through the doped multilayered DBR. Therefore, employing composition grading at the heterointerfaces or small energy band offset heterojunctions can reduce the series resistance [28–30]. On the other hand, it was reported that increasing doping concentration at nodes of the optical field standing wave can avoid the optical absorption and enhance the current transport simultaneously [31].

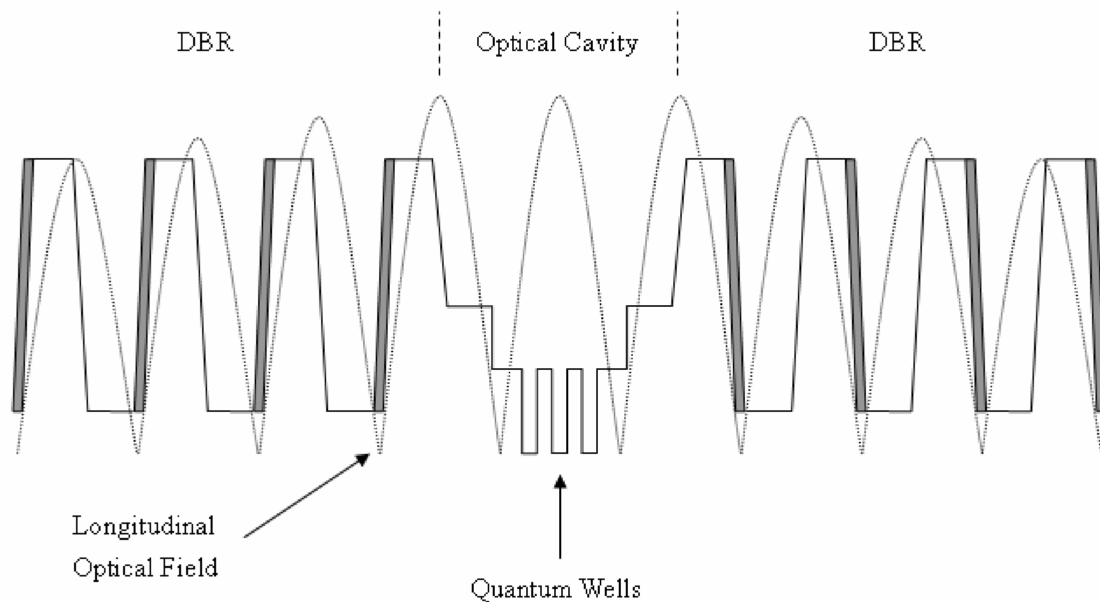

Fig. 1.9. Schematic representation of the relation between conduction band edge energy and longitudinal optical field for a general QW VCSEL structure.

The relation between conduction band edge energy and longitudinal optical field for a general QW VCSEL structure is plotted in Fig. 1.9. The gray areas show the heavily doped regions which are the nodes of the optical field. It is true that considering these design techniques is a complex process to manufacture VCSELs. However, it is noteworthy that a relatively high DBR series resistance will produce a large amount of ohmic heat for VCSELs under CW operation. Under this circumstance, the QW gain spectrum shifts to longer wavelengths and faster than the cavity mode when the device temperature increases due to heating. The spectral misalignment can lead to the degradation of the laser performance. This issue will be discussed in the next subsection about the effects of gain-cavity alignment on the properties of VCSELs.

1.1.3 Gain/Cavity Resonance Alignment

The characteristics of VCSELs are fundamentally different from edge-emitting lasers due to their shorter cavity length, as mentioned in Sec. 1.1. Unlike edge-emitting lasers, VCSELs generally have only one cavity mode in the QW gain spectrum. Therefore, the spectral alignment between the single longitudinal mode and the laser gain spectrum will influence the laser performance profoundly [32]. Figure 1.10 (a) depicts the relative spectral alignment between the cavity mode and the laser gain spectrum in a VCSEL [33]. It can be found that the minimum threshold current can be

obtained as the cavity mode falls at the peak of the gain spectrum.

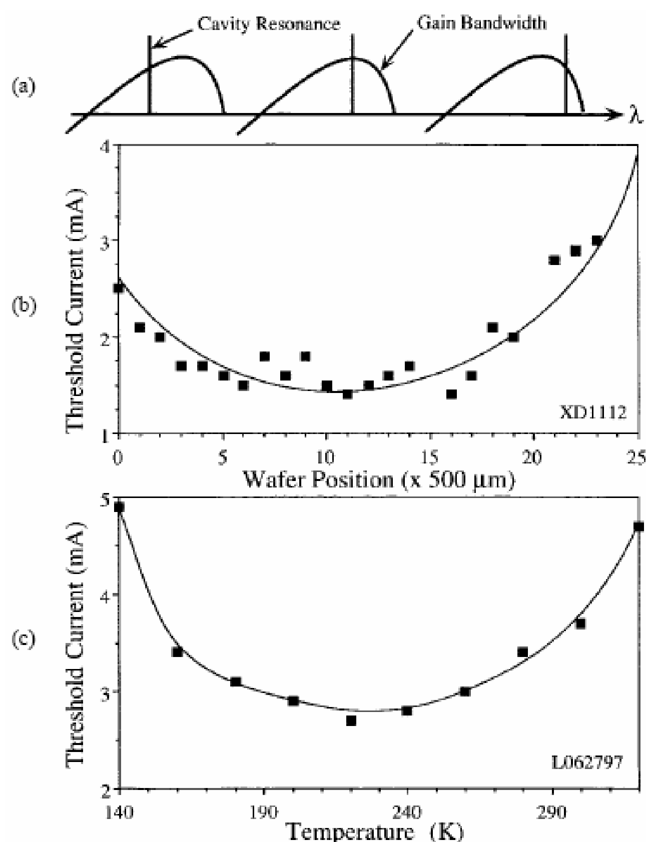

Fig. 1.10. (a) Schematic representation of the spectral alignment between the cavity mode and the gain spectrum in a VCSEL. (b) Variations in VCSEL threshold current caused due to the different thicknesses of the cavity across a wafer. (c) Variations in VCSEL threshold current for a given VCSEL as a function of substrate temperature. (After Ref. 33)

For a Fabry-Perot optical resonator, the cavity resonance wavelength is influenced by the optical thickness of the cavity. Figure 1.10 (b) shows the threshold current of VCSELs located at various locations from a particular wafer designed to exhibit different optical thicknesses of the cavity across

the wafer. Since the QW gain spectrum is not affected for the VCSELs at different wafer locations, the changes in the threshold current are due to the different optical thicknesses of the cavity which make the spectral misalignment between the cavity mode and the gain spectrum. For practical applications, it is necessary to note that both the cavity mode and gain spectrum shift to longer wavelength with increasing temperature due to the temperature-dependent refractive index and energy bandgap, respectively. The cavity mode changes with temperature at roughly 0.8 Å/°C while the gain peak shifts at about 3.3 Å/°C [34]. Therefore, it is possible to make a VCSEL which exhibits a flat threshold current versus temperature behavior over some range of temperature operation, as shown in Fig. 1.10 (c).

In order to obtain a VCSEL with low-temperature-dependent threshold current, the cavity mode is not aligned with the peak gain of the QW at room temperature. Specifically, the cavity mode is often intentionally designed to be at a slightly longer wavelength relative to the peak laser gain at room temperature. As the device heats, the peak laser gain shifts into alignment with the cavity mode to provide optimum VCSEL performance. However, the device temperature increases with increasing operating current. It can be expected that the VCSEL output power is limited by the temperature-induced misalignment at higher operating temperatures [32]. Consequently, the gain-cavity alignment within a VCSEL can be engineered to obtain low threshold current or high output power at a particular temperature. On the other hand, a VCSEL with relatively

invariant threshold currents in a range of operation temperature can also be designed by choosing appropriate gain-cavity alignment at room temperature.

1.1.4 MBE and MOVPE Growth Techniques

Epitaxial growth of VCSELs is very demanding due to the requirement of sufficiently accurate thickness and composition control of each layer. To obtain high performance VCSELs, the reflectance wavelengths of the top and bottom DBR mirrors, the cavity mode wavelength, and the laser gain peak must all be aligned at a specific wavelength for practical VCSEL operation [33]. Therefore, any serious errors caused during the epitaxial growth will result in the degradation of the VCSEL performance. Furthermore, the doping profile and doping concentration control in each layer and in each interface are also critical due to the consideration of DBR series resistance and optical absorption, as mentioned in Sec. 1.1.3. Such complex epitaxy needs stable and reproducible growth methods.

Conventional compound semiconductor epitaxy techniques, such as liquid-phase epitaxy (LPE) and hydride vapor-phase epitaxy (HVPE) can not provide the requisite precision and stability for the epitaxy of VCSELs. Nowadays, there are two powerful epitaxy techniques, i.e., molecular beam epitaxy (MBE) and metalorganic vapor-phase epitaxy (MOVPE), which have been employed in fabricating most optoelectronic devices. For this

reason, both MBE and MOVPE will be described and compared briefly in this subsection.

A. Molecular Beam Epitaxy (MBE)

MBE growth technique was developed in the early 1970s for growing III-V compound semiconductors as well as several other materials [35]. The epitaxy process is achieved in an ultrahigh-vacuum (UHV) environment through the reaction of multiple molecular beams provided from thermally evaporated elemental sources. In this UHV chamber, the mean free path of a free molecule is long enough to prevent the scattering.

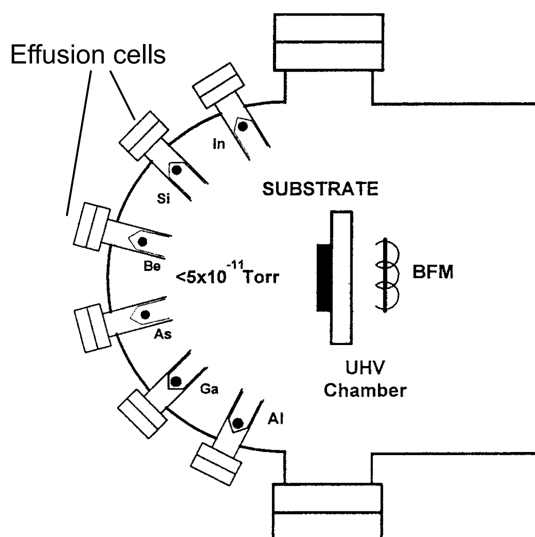

Fig. 1.11. Schematic diagram of MBE growth reactor. (After Ref. 1)

A typical MBE system is illustrated schematically in Fig. 1.11 [1]. Growth materials are contained separately in effusion cells with elemental form. The substrate is heated and rotated during growth to reduce the

effects of molecular beam non-uniformity. Since the growth rates of MBE are typically on the order of a few Å/s, very accurate control of the growth thickness and alloy composition and the more abrupt heterojunction can be achieved.

In the processes of growing VCSEL structures in MBE facilities, because a full VCSEL device requires about 7 μm of epitaxial growth, the relative slow growth rate will take a lot of time to complete. On the other hand, the composition grading and specific doping profile are difficult to realize since the mass flux is mainly dependent on the temperature of the effusion cells. However, the critical advantages for VCSELs grown by MBE system are the superior precision and control [36, 37]. Therefore, there are many research organizations and academic laboratories using MBE for the research and development of VCSELs and other optoelectronic devices.

B. Metalorganic Vapor-phase Epitaxy (MOVPE)

Metalorganic vapor-phase epitaxial growth technique is also known as metalorganic chemical vapor deposition (MOCVD). Fundamental principles of MOVPE growth about III-V semiconductor alloys are reviewed by Ludowise [38]. At present, MOVPE are widely used in industry to fabricate commercial optoelectronic devices due to the relatively rapid growth rate and high wafer throughput [33]. A simplified schematic illustration of a MOVPE system is shown in Fig. 1.12 [1]. Unlike

MBE growth technique, the source materials are metalorganic and hydride precursor gases. Specifically, group V precursors are usually hydrides, including arsine (AsH_3) and phosphine (PH_3), whereas group III sources are metalorganic compounds, such as trimethylgallium (TMGa), trimethylaluminum (TMAl), and trimethylindium (TMIn). Dopant sources for *n*- and *p*-type materials of VCSELs are usually obtained from disilane (Si_2H_6) and carbontetrabromide (CBr_4), respectively. The growth temperature mainly depends on the type of semiconductor compounds. In general, it is typically between 500 °C and 700 °C [39]. Epitaxial layers are formed when the growth precursors decompose on contact with the heating substrate.

In the case of using MOVPE system for VCSEL growth, the faster growth rate and the ease of continuous composition grading are specific advantages of MOVPE. The early VCSEL development focused on the use of MBE for growth. However, high series resistance originating in the abrupt heterojunction of DBR interfaces was the main challenge [40, 41]. On the contrary, Zhou *et al.* first reported high performance VCSEL grown using MOVPE with continuous grading in the DBR and extensive use of C for p–doping in 1991 [42]. Furthermore, a relatively simple *in situ* optical reflectance technique has been developed and adopted to provide an accurate calibration for MOVPE [43, 44]. The composition and growth rate of epitaxial layers can be indicated through the reflectance at the growth surface. On the other hand, any unusual growth conditions can be

immediately found during the growth of VCSELs as well. In conclusion, the advantages for VCSEL growth by MOVPE include wafer uniformity, growth reproducibility, *in situ* monitoring, rapid growth rate, and high-volume manufacturing.

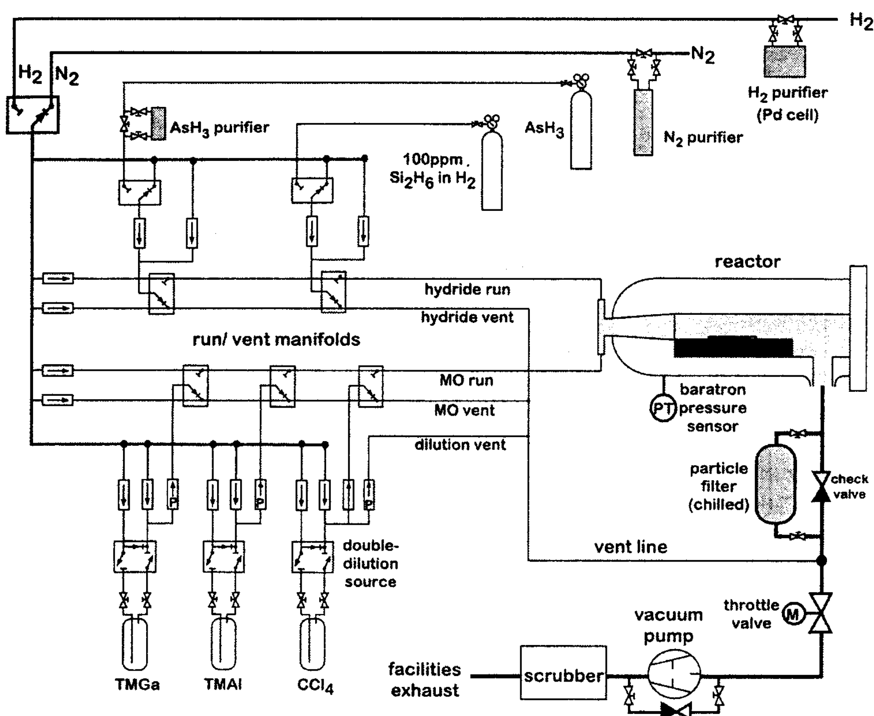

Fig. 1.12. Schematic illustration of a MOVPE system. (After Ref. 1)

1.2 Theoretical Considerations

In this subsection, the theoretical fundamentals relevant to this study are briefly described. First of all, the most popular multiband *k·p* method, which is widely used to calculate the band structure in optoelectronics, is introduced in Sec. 1.2.1. Then, the calculation of optical gain spectrum with valence-band-mixing effects is discussed in Sec. 1.2.2. Section 1.2.3 outlines the effect of strain on the band structures of semiconductors. Finally, the mathematical description for the critical thickness of strained quantum wells is covered at the end of this subsection.

1.2.1 Band Structure: The *k·p* Method

The properties of electrons inside semiconductors are described by the solution of the Schrödinger equation. The solutions provide the electronic band structure and the corresponding wave functions. In order to understand the optical properties of semiconductors, such as absorption or gain spectrum, it is necessary to know the electronic band structure and the electron wave function.

While many techniques, including the tight binding method, the pseudopotential method, the orthogonalized plane wave method, and the multiband *k·p* method, can be used to calculate band structures, for most III-V direct bandgap semiconductors, the band structure near the Γ point is

more important. Under this circumstance, the $k{\cdot}p$ method is a useful and easier technique for analyzing the band structure near Γ point. Therefore, we will focus on the description of the multiband $k{\cdot}p$ method due to its simpler calculation and considerably accurate results near the band edge [45].

In this work, we discuss the $k{\cdot}p$ method which is developed based on the theory of Luttinger-Kohn [46, 47]. Employing the Pikus-Bir Hamiltonian for a strained semiconductor in the Luttinger-Kohn model [26], the valence band structure of a strained bulk semiconductor, which includes the coupling of the heavy-hole (HH), the light-hole (LH), and the spin-orbit split-off (SO) bands, can be described by a 6×6 Hamiltonian in the envelope-function space [48]. For most III-V optoelectronic materials with zincblende structure, the epitaxial layers are typically grown on a (001)-oriented (z-axis) substrate. Under this circumstance, the strain tensor has the following components [48]

$$\begin{aligned} \varepsilon_{xx} &= \varepsilon_{yy} = \frac{a_0 - a}{a} \\ \varepsilon_{zz} &= -\frac{2C_{12}}{C_{11}}\varepsilon_{xx} \\ \varepsilon_{xy} &= \varepsilon_{yz} = \varepsilon_{zx} = 0 \end{aligned} \tag{1.2.1}$$

where a_0 is the lattice constant of the substrate and a is the lattice constant of the layer material. C_{11} and C_{12} are the elastic stiffness constants. On the other hand, for simplicity the 6×6 Hamiltonian can be transformed into a

block-diagonalized Hamiltonian under axial approximation [48, 49].

$$H^{v}(k)=\begin{bmatrix} H^{U}_{3\times3}(k) & 0 \\ 0 & H^{L}_{3\times3}(k)\end{bmatrix},$$

$$H^{\sigma}_{3\times3}(k)=-\begin{bmatrix} P+Q-V_h(z) & R_k \mp iS_k & \sqrt{2}R_k \pm \frac{i}{\sqrt{2}}S_k \\ R_k \pm iS_k & P-Q-V_h(z) & \sqrt{2}Q \pm i\sqrt{\frac{3}{2}}S_k \\ \sqrt{2}R_k \mp \frac{i}{\sqrt{2}}S_k & \sqrt{2}Q \mp i\sqrt{\frac{3}{2}}S_k & P+\Delta(z)-V_h(z)\end{bmatrix}, \quad (1.2.2)$$

where

$$\begin{aligned} &P=P_k+P_\varepsilon, \quad Q=Q_k+Q_\varepsilon, \\ &P_k=\left(\frac{\hbar^2}{2m_0}\right)\gamma_1\left(k_t^2+k_z^2\right), \\ &Q_k=\left(\frac{\hbar^2}{2m_0}\right)\gamma_2\left(k_t^2-2k_z^2\right), \\ &R_k=\left(\frac{\hbar^2}{2m_0}\right)\sqrt{3}\left(\frac{\gamma_2+\gamma_3}{2}\right)k_t^2, \\ &S_k=\left(\frac{\hbar^2}{2m_0}\right)2\sqrt{3}\gamma_3 k_t k_z, \\ &P_\varepsilon=-a_v(\varepsilon_{xx}+\varepsilon_{yy}+\varepsilon_{zz}), \\ &Q_\varepsilon=-\frac{b}{2}(\varepsilon_{xx}+\varepsilon_{yy}-2\varepsilon_{zz}), \end{aligned} \quad (1.2.3)$$

$V_h(z)$ is the unstrained valence band edge; k_t is the wave vector in the plane

of the quantum well; a_v and b are the deformation potentials; $\Delta(z)$ is the spin-orbit split-off energy; γ_1, γ_2, and γ_3 are the Luttinger parameters. In general, the reference energy is taken to be the top of the unstrained valence band in the well region. The upper and lower signs in (1.2.2) are for $\sigma = U$ and $\sigma = L$, respectively. For QW structure, k_z is replaced by $-i(d/dz)$.

In this work, the valence band structures are obtained by solving (1.2.2) with a finite difference method for its simplicity. The differential operators can be transformed into an algebraic equation by using finite difference formulas. The detailed description can be obtained in ref. 50.

1.2.2 Optical Gain Model

The optical gain spectrum of quantum-well lasers is an important property to determine the threshold condition. Early, the simplified model for the calculation of gain spectra is based on the parabolic band structures, which neglects the coupling between the HH and LH subbands. However, in quantum wells, valence-band-mixing effects among the HH, LH, and SO subbands should be considered and the subband structures can be highly non-parabolic, especially for strained quantum wells [26]. The differences of the calculated optical gain spectra between the parabolic and non-parabolic band models had been compared in refs. 51 and 52. It was found that the gain spectra based on the non-parabolic band model showed remarkable differences in both spectral shape and peak amplitude as

compared with those based on the conventional parabolic band model. Furthermore, the peak gain was reduced markedly and the gain spectrum was more symmetric in the results of the non-parabolic band model, which is in more agreement with the experimental shapes of gain spectra [51].

Because of this reason, in this work the valence-band-mixing effect is taken into account in the calculation of quantum-well gain spectra. Specifically, the optical gain spectra are calculated based on the valence band structures which are obtained by solving the eigenvalues of the 6×6 Hamiltonian for different k_t values. Therefore, the optical gain spectra of single-quantum-well structures can be expressed by [26, 49]

$$g(\hbar\omega) = g_0 \frac{2}{L_z} \sum_{\sigma} \sum_{n,m} \int_0^{\infty} \left| \hat{e} \cdot \mathrm{M}_{nm}^{\sigma}(k_t) \right|^2 \frac{(\Gamma / \pi)}{(E_{\sigma,nm}^{cv}(k_t) - \hbar\omega)^2 + \Gamma^2}$$

$$\times (f_n^c(k_t) - f_{\sigma m}^v(k_t)) \frac{k_t \mathrm{d}k_t}{2\pi}, \tag{1.2.4}$$

where

$$g_0 = \frac{q^2 \pi}{n c \varepsilon_0 m_0^2 \omega}, \tag{1.2.5}$$

$$f_n^c(k_t) = \frac{1}{1 + \exp\left(\frac{E_n^c(k_t) - F_c}{k_B T} \right)}, \tag{1.2.6}$$

$$f_{\sigma m}^v(k_t) = \frac{1}{1 + \exp\left(\frac{E_{\sigma,m}^v(k_t) - F_v}{k_B T} \right)}, \tag{1.2.7}$$

$$E^{cv}_{\sigma,nm}(k_t) = E^c_n(k_t) - E^v_{\sigma,m}(k_t)\,. \tag{1.2.8}$$

F_c and F_v are the quasi-Fermi levels for electrons and holes, q is the magnitude of the electron charge, $\hbar$ is the reduced Planck's constant, n is the refractive index of the quantum well, ε_0 is the free-space dielectric constant, c is the speed of light, $\mathrm{M}^{\sigma}_{nm}(k_t)$ is the momentum matrix element in the quantum well, L_z is the thickness of quantum well, $\Gamma = \hbar/\tau$ is the broadening due to intraband scattering relaxation time τ, $E^c_n(k_t)$ is the nth conduction subband, $E^v_{\sigma,m}(k_t)$ is the mth valence subband from the $k{\cdot}p$ calculation. The indices n and m denote the electron states in the conduction band and the heavy hole or light hole subband states in the valence band, respectively.

The spontaneous emission rate can be given by [26, 49]

$$r_{sp}(\hbar\omega) = r_0 \frac{2}{L_z} \sum_{\sigma} \sum_{n,m} \int_0^{\infty} \left|\mathrm{M}_{\mathrm{sp}}(k_t)\right|^2 \frac{(\Gamma/\pi)}{(E^{cv}_{\sigma,nm}(k_t) - \hbar\omega)^2 + \Gamma^2}$$

$$\times f^c_n(k_t)(1 - f^v_{\sigma m}(k_t)) \frac{k_t \mathrm{d}k_t}{2\pi}\,, \tag{1.2.9}$$

where

$$r_0 = \frac{q^2 n \omega}{\pi \hbar c^3 \varepsilon_0 m_0^2}\,, \tag{1.2.10}$$

$$\left|\mathrm{M}_{\mathrm{sp}}\right|^2 = \frac{1}{3}\left(2\left|\mathrm{M}_{\mathrm{TE}}\right|^2 + \left|\mathrm{M}_{\mathrm{TM}}\right|^2\right). \tag{1.2.11}$$

Since the spontaneous emission is randomly polarized, the momentum matrix element of the spontaneous emission is the average of two TE polarization components and one TM polarization component.

1.2.3 Strain Effects

It has been suggested that the performance of semiconductor lasers can be improved by employing a strained quantum-well structure [53, 54]. This technique is particularly simple for a practical epitaxy. When a well layer has a larger native lattice constant than a barrier layer, the lattice of the well layer is compressed in the plane of the well to match that of the barrier layer. Furthermore, the lattice constant in the direction normal to the plane is elongated. This condition is illustrated in Fig. 1.13. Since the band structure is related to the symmetry of the crystal structure, it can be expected that the strain-induced distortion in crystal structure should lead to alterations in the band structure.

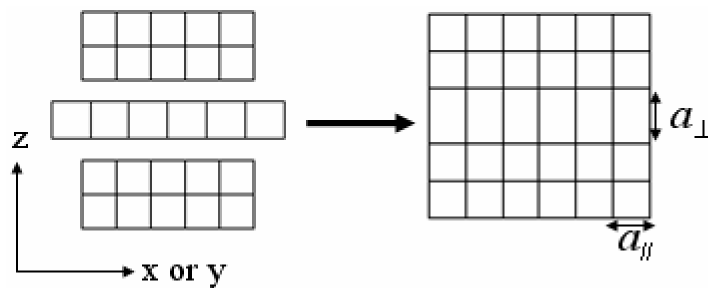

Fig. 1.13. Crystal lattice deformation under compressive strain. The z axis represents the quantum-well growth direction.

Corzine *et al.* compared the band structures, optical gain, and threshold properties for an unstrained $GaAs/Al_{0.2}Ga_{0.8}As$ QW and a compressively strained $In_{0.2}Ga_{0.8}As/Al_{0.2}Ga_{0.8}As$ QW theoretically [55]. The calculated valence subband structure of an unstrained 80 Å $GaAs/Al_{0.2}Ga_{0.8}As$ QW is showed in Fig. 1.14. It is apparent that the valence-band-mixing effect between the HH and LH subbands results in the dramatically non-parabolic valence subband structure. In addition, the density of states of the subbands is also shown in Fig. 1.14, where $\rho_v(E)/\rho_c(E)$ is the density of states in valence subbands relative to the density of states in the first conduction subband. It is observed that ρ_v is roughly $2.5\rho_c$ near the band edge. However, it increases rapidly with the higher energy especially as the mixing effect between the subbands starts to become significant.

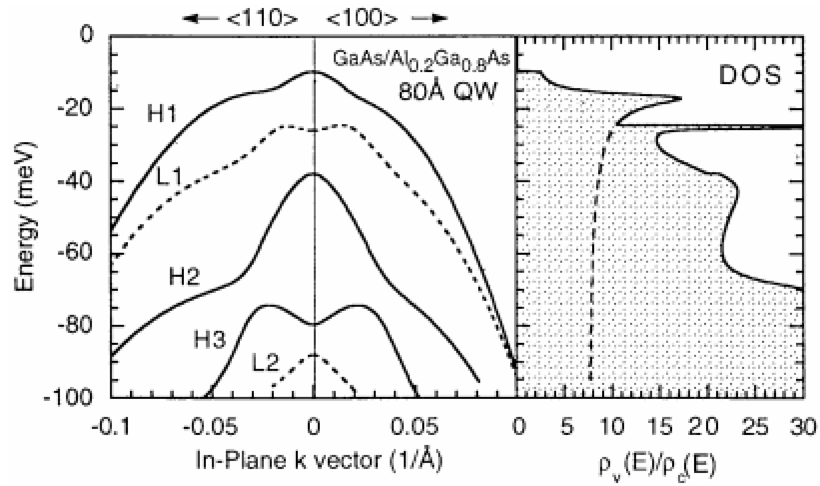

Fig. 1.14. The valence subband structure of an 80 Å $GaAs/Al_{0.2}Ga_{0.8}As$ quantum well and the total (solid curve) and H1 subband (dashed curve) density of states plotted relative to the density of states in the first conduction (C1) subband. (After Ref. 55)

To understand how the strained quantum wells improve the laser performance, an 80 Å $In_{0.2}Ga_{0.8}As/Al_{0.2}Ga_{0.8}As$ QW, which has a corresponding compressive strain of 1.4%, is compared with the previous $GaAs/Al_{0.2}Ga_{0.8}As$ QW. Figure 1.15 shows the valence subband structure and the density of states of the 80 Å $In_{0.2}Ga_{0.8}As/Al_{0.2}Ga_{0.8}As$ QW [55]. It can be seen clearly that the compressive strain separates the HH and LH subbands and pushes the LH subbands out of the energy scale shown in Fig. 1.15. Therefore, the band-mixing effect is greatly reduced near the band edge, which decreases the density of states in the valence band edge. In comparison with Fig. 1.14, the density of states in compressively strained $In_{0.2}Ga_{0.8}As$ QW is reduced significantly and matching between ρ_c and ρ_v is greatly improved.

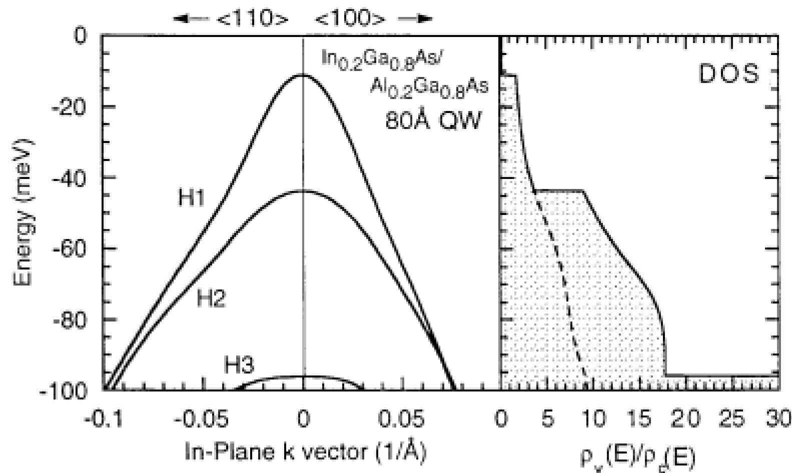

Fig. 1.15. The valence subband structure of an 80 Å $In_{0.2}Ga_{0.8}As/Al_{0.2}Ga_{0.8}As$ quantum well and the total (solid curve) and H1 subband (dashed curve) density of states plotted relative to the density of states in the first conduction (C1) subband. (After Ref. 55)

1.2.4 Critical Thickness for Strained Layer

In an epitaxial process, if quantum-well layers are grown on a substrate with the same lattice constant, the number and thickness of the quantum wells are not design constraints. Nevertheless, in a strained quantum-well layer, the epitaxial thickness should be less than the critical thickness to avoid the existence of misfit dislocations and threading dislocations. These dislocations are detrimental to device performance and lifetime. Accordingly, while the use of strained quantum wells is able to obtain better laser performance, the issue of critical thickness should be considered in the design of strained quantum-well lasers.

A theoretical consideration of the critical layer thickness was proposed by Matthews and Blakeslee based on the mechanical equilibrium model [56, 57]. The formula can be expressed by

$$h_c = \frac{a}{\kappa\sqrt{2}\pi\varepsilon}\frac{1-0.25v}{1+v}\left(\ln\frac{h_c\sqrt{2}}{a}+1\right), \tag{1.2.12}$$

where h_c is the critical thickness, and a is the natural unstrained lattice constant of epitaxial layer. The ε is the mismatch strain defined as

$$\varepsilon = -\frac{a_s - a}{a}, \tag{1.2.13}$$

where a_s is the lattice constant of substrate, and v is Poisson’s ration, which is defined as

$$\nu = \frac{C_{12}}{C_{11} + C_{12}}. \qquad (1.2.14)$$

The coefficient κ has a value of 1 for a strained layer superlattice, 2 for a single quantum well, and 4 for a single strained layer. According to this model, the calculated critical thicknesses for $In_xGa_{1-x}As/GaAs$ as a function of indium composition are shown in Fig. 1.16 for (a) superlattice, (b) quantum well, and (c) single strained layer structures [58].

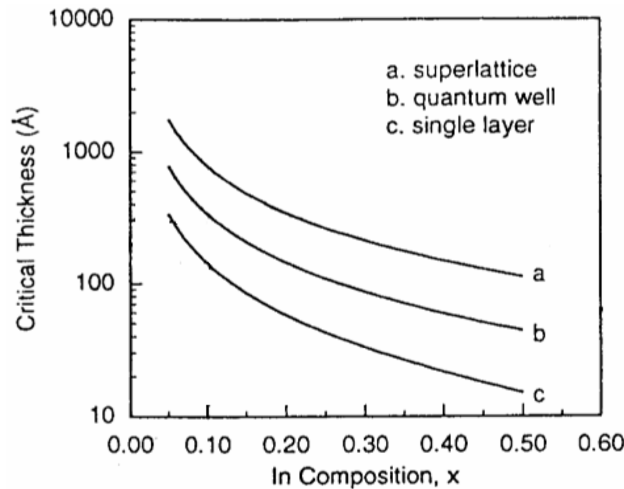

Fig. 1.16. The critical thickness of $In_xGa_{1-x}As/GaAs$ as a function of indium composition calculated by the Matthews and Blakeslee model for (a) superlattice, (b) quantum well, and (c) single strained layer structures. (After Ref. 58)

In addition to the Matthews and Blakeslee model, People and Bean also proposed an alternative formula for the critical thickness of a single layer based on the energy balance model [59, 60]. The expression for the critical thickness for a single strained layer is given by

$$h_c = \frac{a}{32\sqrt{2}\pi\varepsilon^2}\frac{1-\nu}{1+\nu}\left(\ln\frac{h_c\sqrt{2}}{a}\right), \tag{1.2.15}$$

where a, ν, ε, and h_c have the same definition as the Matthews and Blakeslee model. Figure 1.17 shows the comparison of the computed critical thicknesses for $In_xGa_{1-x}As$/GaAs single layers as a function of indium composition by Matthews and Blakeslee model and People and Bean model, respectively. It can be found that the calculated results are different markedly, especially at lower indium composition.

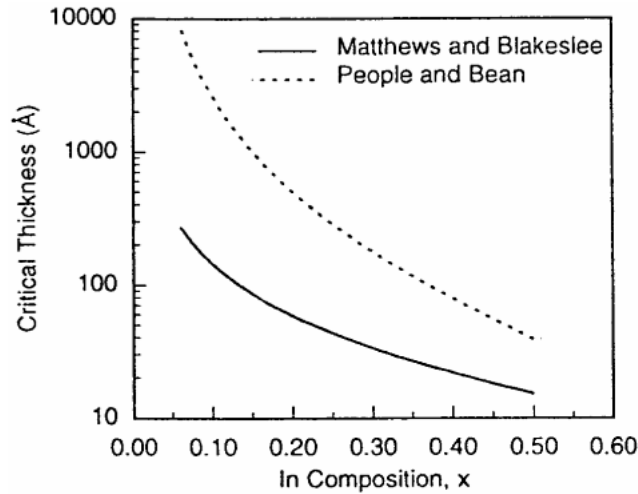

Fig. 1.17. Comparison of the calculated critical thicknesses for $In_xGa_{1-x}As$/GaAs single layers as a function of indium composition according to the Matthews and Blakeslee model and the People and Bean model. (After Ref. 58)

For $In_xGa_{1-x}As$/GaAs quantum-well structures, the calculated critical thicknesses by the Matthews and Blakeslee model have shown reasonable agreement with the experimentally measured results [61–64]. In addition,

the Matthews and Blakeslee model has been used to evaluate the critical thickness of many material systems as well [65–68]. Therefore, we will employ this model to compute the critical thicknesses in the subsequent chapter.

Chapter 2. Optimization Study of the InGaAlAs Quantum-Well Structures for 850-nm VCSELs

Currently high-performance 850-nm vertical-cavity surface-emitting lasers have been employed in short distance optical interconnects. VCSELs offer well-known advantages including circular output beam, low threshold current, high modulation bandwidth, single longitudinal mode, and manufacturing advantages such as on-wafer testing [33, 69, 70]. These virtues make VCSEL an ideal light source for high-speed optical communication [71−73]. The 850-nm VCSELs usually utilize an unstrained GaAs/AlGaAs quantum well as the active layer structure. Nevertheless, it has been shown that semiconductor lasers with a lower threshold current density and higher modulation speed can be achieved by using a strained quantum-well structure, which is due to the reduced effective mass of the heavy-hole subband in the plane of the quantum well, as described in Sec. 1.2.3 [53, 54, 74, 75]. Therefore, the optimization study of the strained quantum-well structures for 850-nm VCSELs is necessary for achieving optimal laser performance.

In this chapter, the published literatures on strained 850-nm InGaAs and InGaAlAs VCSELs are firstly reviewed. Furthermore, the optimal strain level of compressively strained InGaAlAs/AlGaAs quantum wells will be studied for 850-nm VCSELs by using the PICS3D (Photonic Integrated Circuit Simulator in 3D) simulation program [76].

2.1 Study Related to the Compressively Strained 850-nm InGaAlAs VCSELs

Generally speaking, 850-nm VCSELs usually utilize an unstrained GaAs/AlGaAs quantum well as the active layer structure for simplicity in epitaxial growth. In order to obtain strained quantum wells with the emission wavelength at 850 nm, the choice of the active region grown on GaAs substrate includes InGaAs/AlGaAs, InGaAlAs/AlGaAs, and InGaAsP/InGaP material systems. Several compressively strained InGaAs/AlGaAs semiconductor lasers with very low threshold current were demonstrated [75, 77]. However, to emit at 850 nm, the amount of compressive strain is limited due to the thinner quantum wells. As for the InGaAlAs/AlGaAs material system, by incorporating appropriate aluminum and indium compositions into GaAs QW structures, the desired emission wavelength and strain level can be achieved simultaneously for potential improvements in laser performance. Experimentally, compressively strained InGaAlAs/AlGaAs 850-nm VCSELs with very low thresholds have been reported [78−81] even if the epitaxial process of the InGaAlAs material may induce the problem of oxygen impurity. Moreover, the compressively strained InGaAlAs quantum wells emitting near 850 nm are mostly discussed for conventional laser diodes [82−86]. As for the numerical analysis of the properties of compressively strained InGaAlAs quantum wells, although the strained $(Al_xGa_{1-x})_yIn_{1-y}As_zP_{1-z}$ material

system was investigated in an attempt to improve the optical performance of 850-nm lasers, the amount of compressive strain of those quantum wells were fixed at 1.7% and 0.6% for InGaAlAs and InGaAs quantum wells respectively [87]. To the best of our knowledge, qualitative analysis of varying compressive strain in InGaAlAs quantum wells which have an emission wavelength of approximately 850 nm has not been well documented in literature. The InGaAsP/InGaP material system with an emission wavelength near 850 nm will be described and discussed in the next chapter.

2.2 Physical model and Parameters

In this study, the calculations are performed assuming that the InGaAlAs active layers are grown on (001) GaAs substrates. Thus, the strained layers are subject to biaxial stress in the surface plane. As for the band structures of the compressively strained InGaAlAs quantum wells, it is assumed that the conduction bands can be characterized by a parabolic-band model, such as the situation of most III-V direct bandgap semiconductors [49]. The nonparabolic valence band structures including the coupling of the heavy hole, light hole, and spin-orbit splitting bands are calculated using a 6×6 Hamiltonian [48]. Except for the unstrained bandgap energies, in order to obtain the numerical parameters required for $k{\cdot}p$ calculations for the InGaAlAs materials, a linear interpolation between the parameters of the relevant binary semiconductors is utilized. For physical parameter P, the interpolation formula is [88]

$$P(In_{1-x-y}Ga_xAl_yAs) = P(InAs)\,(1-x-y) + P(GaAs)\,x + P(AlAs)\,y. \qquad (2.2.1)$$

The material parameters of the binary semiconductors used in this study are summarized in Table 2.1 [45]. The formula for the calculation of unstrained InGaAlAs bandgap energies can be expressed as a weighted sum of the bandgap energies of relevant ternary semiconductors with appropriate bowing parameters. Specifically, the unstrained InGaAlAs bandgap energies are calculated by following expressions [45]

$$E_g(InGaAlAs) = \frac{xyE_g^u(GaAlAs) + yzE_g^v(InAlAs) + xzE_g^w(InGaAs)}{xy + yz + zx}, \quad (2.2.2)$$

$$E_g^u(GaAlAs) = uE_g(AlAs) + (1-u)E_g(GaAs) - u(1-u)B(GaAlAs), \quad (2.2.3)$$

$$E_g^v(InAlAs) = vE_g(InAs) + (1-v)E_g(AlAs) - v(1-v)B(InAlAs), \quad (2.2.4)$$

$$E_g^w(InGaAs) = wE_g(InAs) + (1-w)E_g(GaAs) - w(1-w)B(InGaAs), \quad (2.2.5)$$

$$u = \frac{1-x+y}{2}, \quad v = \frac{1-y+z}{2}, \quad w = \frac{1-x+z}{2}, \quad (2.2.6)$$

where x, y, and $z = 1-x-y$ represent the compositions of gallium, aluminum, and indium in the InGaAlAs material system respectively.

Table 2.1. Parameters of the binary semiconductors GaAs, AlAs, and InAs.

Parameter	Symbol (unit)	GaAs	AlAs	InAs
Lattice constant	a_0 (Å)	5.65325	5.6611	6.0583
Spin-orbit splitting	Δ_{so} (eV)	0.341	0.28	0.39
Luttinger parameter	γ_1	6.98	3.76	20.0
	γ_2	2.06	0.82	8.5
	γ_3	2.93	1.42	9.2
Hydrostatic deformation potential	a (eV)	−8.33	−8.11	−6.08
Shear deformation potential	b (eV)	−2.0	−2.3	−1.8
Elastic stiffness constant	C_{11} (GPa)	1221	1250	832.9
Elastic stiffness constant	C_{12} (GPa)	566	534	452.6
Electron effective mass	m_e/m_o	0.067	0.15	0.026

The bandgap bowing parameters of GaAlAs, InAlAs, and InGaAs are –0.127+1.310y eV, 0.70 eV, and 0.477 eV, respectively [45]. The temperature dependent bandgap energies of the relevant binary semiconductors are calculated using the commonly employed Varshni formula

$$E_g(T) = E_g(T=0) - \frac{\alpha T^2}{T+\beta} . \tag{2.2.7}$$

The values of α, β, and $E_g(T = 0)$, i.e., the bandgap energy at zero Kelvin, of the binary alloys are listed in Table 2.2 [45]. The conduction band offset for the compressively strained InGaAlAs/AlGaAs quantum well is set to 67% of the total band offset [89]. The optical gain spectra of single-quantum-well structures, with the valence-band-mixing effect being taken into account, have been expressed in (1.2.4). To account for the broadening due to scattering, it is assumed that $\tau = 0.1$ ps [52, 90–92] in the calculations.

The spontaneous emission rate is calculated according to (1.2.9). The radiative current density J_{rad} can be calculated from the spontaneous emission spectrum using [26]

$$J_{rad} = ql \int r_{sp}(E)\, dE . \tag{2.2.8}$$

where l is the thickness of the active region. This equation can be used to estimate the injected current density required to achieve laser threshold. If

the laser is without any non-radiative recombination processes such as the Auger recombination and current leakage, under the assumption of unity injection efficiency, the radiative current density is eventually equivalent to the injected current density.

Table 2.2. Varshni parameters of the binary semiconductors GaAs, AlAs, and InAs.

Parameter (unit)	GaAs	AlAs	InAs
α (meV/K)	0.5405	0.885	0.276
β (K)	204	530	93
E_g ($T = 0$) (eV)	1.519	3.099	0.417

2.3 Simulation Result and Discussion

In this work, in order to explore the optical properties and optimal active layer configurations for 850-nm VCSELs, the electronic structures and optical gain spectra of the compressively strained $In_{0.02}Ga_{0.98}As$ and quaternary InGaAlAs quantum wells emitting at 838 nm with variant indium and aluminum compositions are investigated using 6×6 *k·p* Hamiltonian including the heavy hole, light hole, and spin-orbit splitting bands. A gain-cavity detuning of approximately 12 nm is generally utilized for the design of 850-nm VCSELs to result in a flat threshold current versus temperature behavior over some range of temperature operation. Based on this 6×6 *k·p* theory, the transparency carrier densities, transparency radiative current densities, and maximum differential gains for the $In_{0.02}Ga_{0.98}As$ and InGaAlAs quantum wells with different compressive strains are compared and discussed.

To discuss the properties of the 838-nm InGaAlAs quantum wells with different compressive strains, five quantum-well structures including $In_{0.02}Ga_{0.98}As$, $In_{0.08}Ga_{0.883}Al_{0.037}As$, $In_{0.14}Ga_{0.786}Al_{0.074}As$, $In_{0.20}Ga_{0.671}Al_{0.119}As$, and $In_{0.26}Ga_{0.585}Al_{0.155}As$ are systematically studied in this chapter, which have corresponding in-plane compressive strains of 0.143%, 0.575%, 1.004%, 1.497%, and 1.848% respectively. All of the quantum wells have the same thickness of 7 nm and the same barrier layer of $Al_{0.3}Ga_{0.7}As$. Since the lattice constants are nearly identical for GaAs and

AlAs, the strains are dominated by indium composition in InGaAlAs quantum wells. The compressive strain increases when the indium composition in InGaAlAs quantum wells increases. Thus, the indium composition is varied with a fixed step of 6% and the appropriate aluminum composition is chosen in such a way that the emission wavelengths of the $In_{0.02}Ga_{0.98}As$ and InGaAlAs quantum-well structures resulted from transitions between the lowest conduction subband (C1) and the top valence subband (HH1) are 838 nm.

In Figs. 2.1(a)–2.1(e), the valence subband structures for the $In_{0.02}Ga_{0.98}As$ and InGaAlAs quantum wells with variant indium and aluminum compositions are plotted as a function of the in-plane wave vector k_t, which is along the horizontal axis and normalized by $2\pi/a_0$. From these valence-band dispersion curves, it is observed that the degree of band warping is increased due to the increase of indium composition in the quantum wells. Therefore, the effective mass of the holes becomes lighter, which makes the density of states in valence and conduction bands more matched. This is expected to result in a much higher differential gain and lower transparency carrier density. Compared to InGaAlAs quantum wells, the band identifications in $In_{0.02}Ga_{0.98}As$ quantum well are somewhat different. It has the fifth confined hole level (LH2) in addition to the four HH1, HH2, LH1, and HH3 confined levels. The thickness of quantum well, barrier height, and effective mass of holes influence the number of confined energy levels. Higher effective mass, deeper barrier height, and wider

quantum-well thickness increase the number of confined energy levels. On the other hand, the distance of separation between LH1 and HH1 subbands increases with compressive strain in the quantum wells.

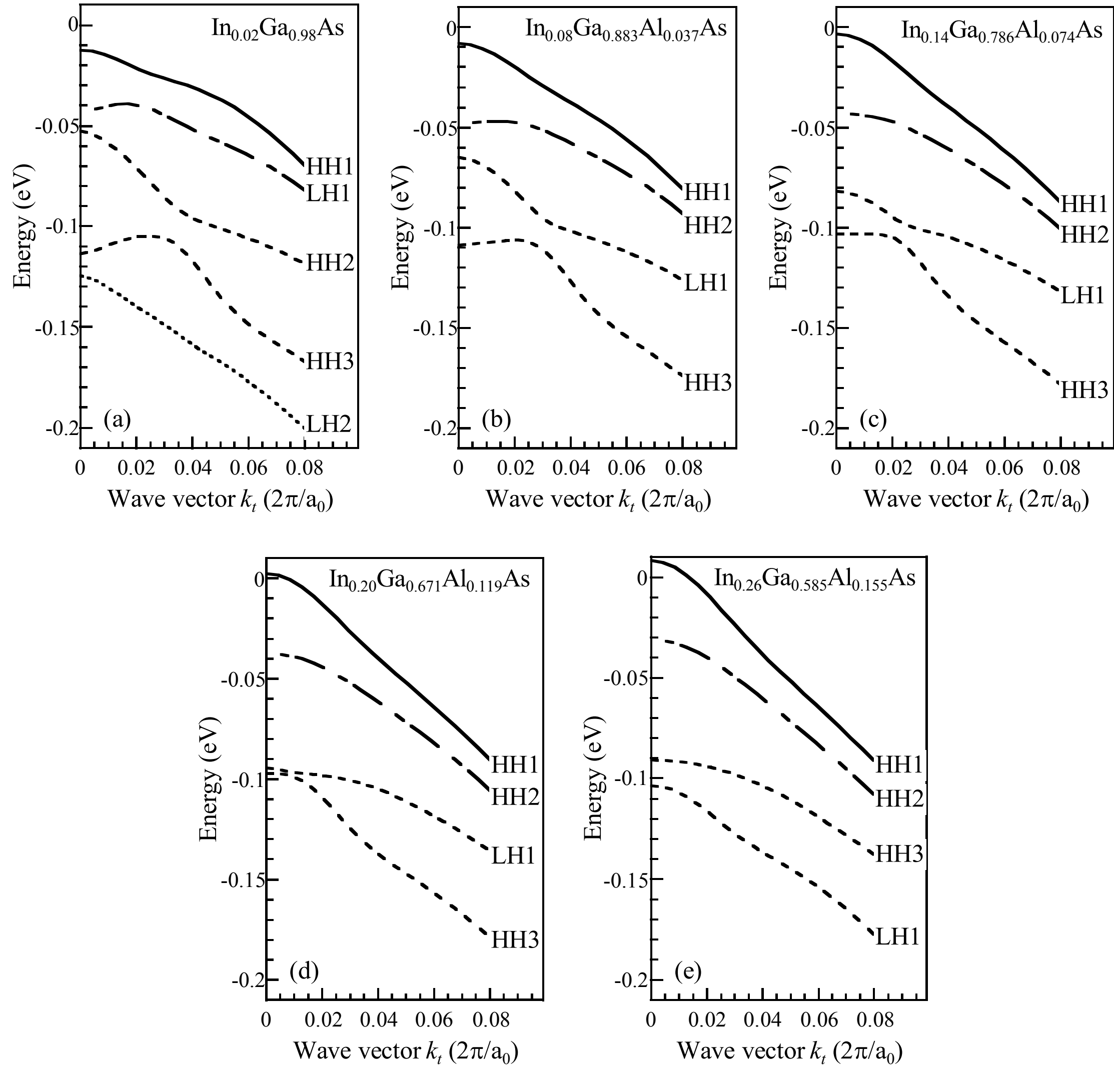

Fig. 2.1. The valence subband structures for 7-nm InGaAlAs quantum well sandwiched between $Al_{0.3}Ga_{0.7}As$ barriers for (a) $In_{0.02}Ga_{0.98}As$, (b) $In_{0.08}Ga_{0.883}Al_{0.037}As$, (c) $In_{0.14}Ga_{0.786}Al_{0.074}As$, (d) $In_{0.20}Ga_{0.671}Al_{0.119}As$, and (e) $In_{0.26}Ga_{0.585}Al_{0.155}As$.

Figure 2.2 shows the room-temperature optical gain spectra of the $In_{0.02}Ga_{0.98}As$ and InGaAlAs quantum wells at a fixed carrier density 6×10^{18} cm^{-3} for TE polarization and TM polarization. The difference of the optical gain between TE and TM modes becomes more evident when the compressive strain is high. This enhanced polarization discrimination is due to the compressive strain which lowers the LH1 band away from the valence band edge. This situation leaves more carriers for the C1-HH1 transitions so that the peak gain for TE mode is higher with more compressive strain in the quantum wells. Note also that, for $In_{0.02}Ga_{0.98}As$ quantum well, there is a second peak in the gain spectrum of TE mode. Because of the smaller separation distance between HH1 and LH1 in $In_{0.02}Ga_{0.98}As$ quantum well, the C1-LH1 transition becomes a more important contribution to the gain spectrum of $In_{0.02}Ga_{0.98}As$ quantum well than those of InGaAlAs quantum wells. Furthermore, when the compressive strain increases, the peak gain of TM mode shifts to the shorter wavelength and has a lower value. It is consistent with the valence subband structures shown in Figs. 2.1(a)–2.1(e). The transition energy of C1-LH1 is larger with more compressive strain in the quantum well and the C1-HH1 transition dominates the optical gain. Furthermore, it is apparent that the InGaAlAs quantum wells have higher TE gain than the $In_{0.02}Ga_{0.98}As$ quantum well. However, it is noteworthy that, further increase in material gain becomes minimal when the compressive strain is higher than approximately 1.5%.

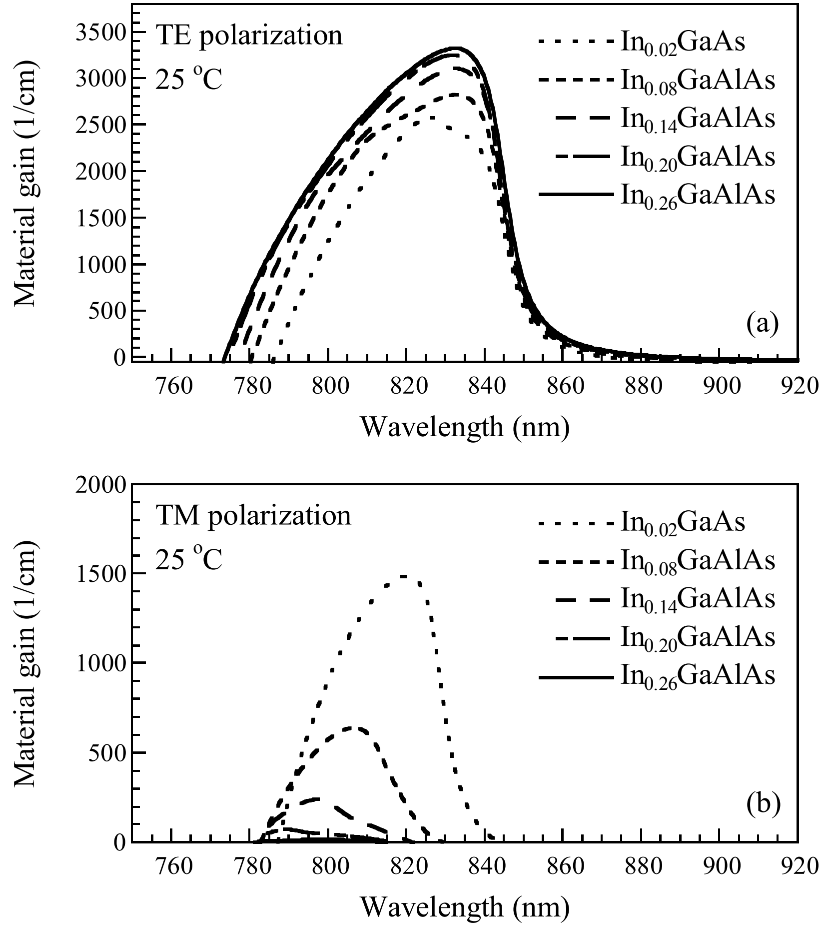

Fig. 2.2. Room-temperature (a) TE and (b) TM gain spectra for compressively strained 7-nm $In_{0.02}Ga_{0.98}As$ and InGaAlAs quantum wells with $Al_{0.3}Ga_{0.7}As$ barrier. The input carrier concentration is 6×10^{18} cm^{-3}.

Figure 2.3 shows the peak material gain as a function of carrier density for $In_{0.02}Ga_{0.98}As$ and InGaAlAs quantum wells at 25 °C and 95 °C. We solely compare the TE mode of different quantum-well structures because the TM mode is strongly depressed with high compressive strain in the quantum wells. Besides, the TM mode is mainly introduced by C1-LH1 transition which provides shorter emitting wavelength than 838 nm. When

the compressive strain increases, the transparency carrier density decreases. Note that the higher valence band curvature in the compressively strained quantum well results in smaller joint densities of states, which makes the creation of population inversion easier [93]. In addition, the gain peak is higher with the compressive strain in the quantum wells in the range of the calculated carrier concentration. Similar trend is observed when the temperature is 95 °C.

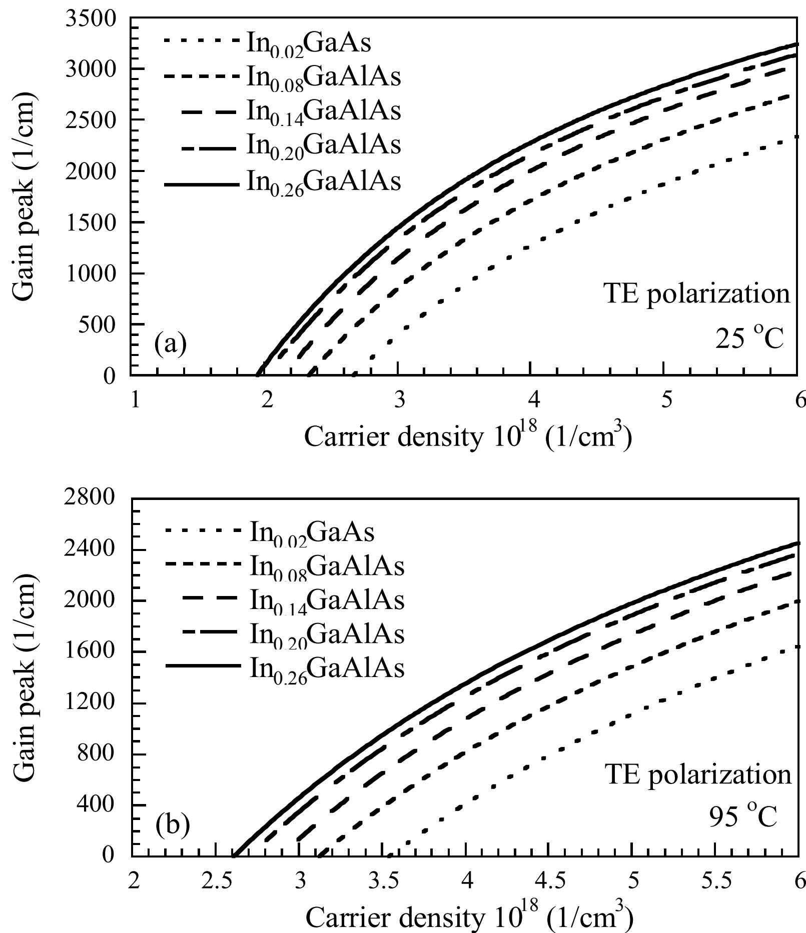

Fig. 2.3. Gain peak of TE mode as a function of carrier density for $In_{0.02}Ga_{0.98}As$ and variant InGaAlAs quantum wells with $Al_{0.3}Ga_{0.7}As$ barrier at (a) 25 °C and (b) 95 °C.

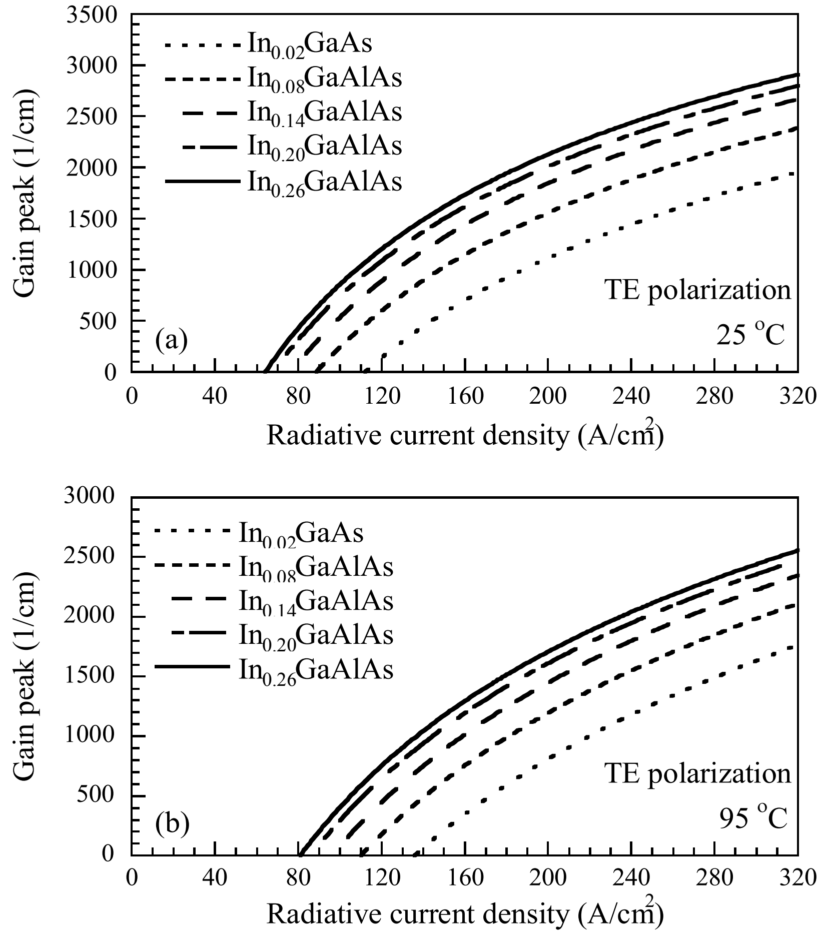

Fig. 2.4. Gain peak of TE mode as a function of radiative current density for $In_{0.02}Ga_{0.98}As$ and variant InGaAlAs quantum wells with $Al_{0.3}Ga_{0.7}As$ barrier at (a) 25 °C and (b) 95 °C.

Figure 2.4 depicts the peak material gain of TE mode as a function of radiative current density for $In_{0.02}Ga_{0.98}As$ and InGaAlAs quantum wells at 25 °C and 95 °C. The transparency radiative current density decreases when the composition of indium in quantum wells increases. It is concluded from Figs. 2.3 and 2.4 that, higher compressive strain in quantum wells results in lower transparency carrier density and transparency radiative current

density and higher peak of gain. However, it should be noted that, the peak of gain in the range of calculated carrier density and radiative current density does not have evident variation when the indium composition is higher than about 20%, which has a corresponding compressive strain of approximately 1.5%.

For convenient comparison among the characteristics of $In_{0.02}Ga_{0.98}As$ and InGaAlAs quantum wells with different compressive strains, the transparency carrier densities and transparency radiative current densities at 25 °C and 95 °C are plotted as a function of the compressive strain in quantum wells in Fig. 2.5. Note that the decrease of transparency carrier density and transparency radiative current density with an increase in compressive strain at 25 °C and 95 °C becomes less evident when the compressive strain in quantum wells is higher than approximately 1.5%. This can be explained with the band structures of InGaAlAs quantum wells shown in Fig. 2.1. It can be found that the band curvature of the HH1, which dominates the transition in the valence band, does not vary obviously when the compressive strain is higher than 1.5%. It indicates that the density of states near the top of valence band do not change markedly when the compressive strain in quantum wells is higher than 1.5%. Moreover, because the transparency carrier density depends primarily on the Bernard-Duraffourg inversion condition [74]

$$\left(F_c - F_v\right) > \hbar\omega \geq E_g \,, \qquad (2.3.1)$$

which requires that the separation between quasi-Fermi levels be greater than the bandgap, the factor of $F_c - F_v$ is sensitive to the density of states near the top of valence band when the carriers are injected into the quantum wells. Therefore, the properties of the InGaAlAs quantum wells under study do not change markedly when the compressive strain in quantum wells is higher than approximately 1.5%.

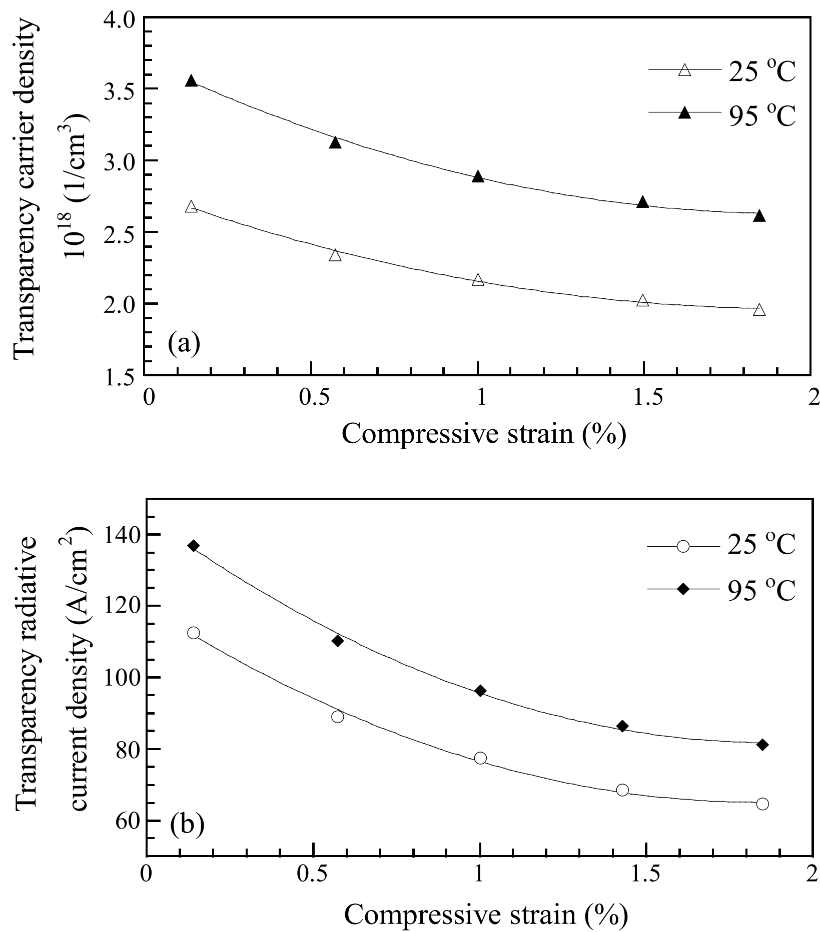

Fig. 2.5. (a) Transparency carrier density and (b) transparency radiative current density of TE mode as a function of compressive strain at 25 °C and 95 °C.

For semiconductor lasers as a light source of high-speed optical communication systems, the differential gain is one of the most important parameters. This is primarily because the relaxation resonance frequency of the laser depends on the square root of the differential gain [49]. Therefore, the differential gain of the InGaAlAs quantum wells is discussed. Figure 2.6 depicts the maximum differential gain as a function of the compressive strain in quantum wells at 25 °C and 95 °C. It can be found that the maximum differential gain increases with the compressive strain in quantum wells. It is interesting to note that, the increase of maximum differential gain with more compressive strain in quantum wells becomes less evident when the compressive strain is higher than approximately 1.5% as well. Therefore, the variation of valence subband structures with the amount of compressive strain in quantum wells still plays an important role for the differential gain of InGaAlAs quantum wells.

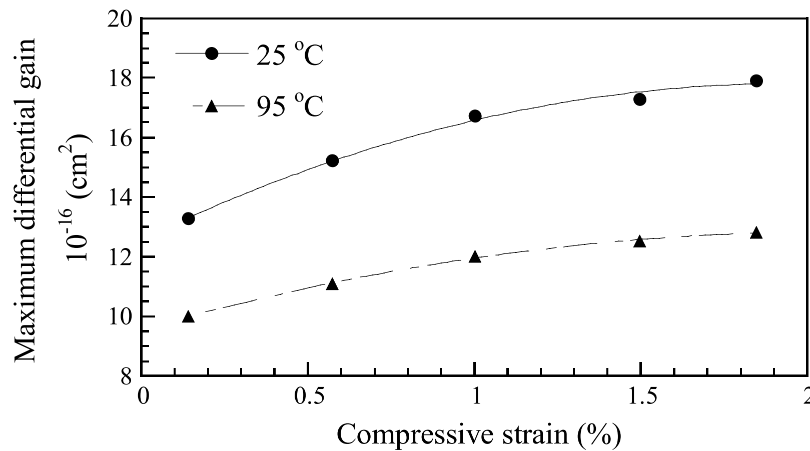

Fig. 2.6. Maximum differential gain of TE mode as a function of compressive strain at 25 °C and 95 °C.

It needs to be mentioned here that, although the optical properties of compressively strained InGaAlAs quantum wells can be improved by employing larger amount of compressive strain in quantum wells, a higher level of strain in quantum wells may have crystal quality concerns. The Matthews and Blakeslee model, which has been described in Sec. 1.2.4, is employed to estimate the critical thicknesses of the five quantum-well structures under study. In the calculations, the lattice constants and elastic constants are taken from Table 2.1. The results of the calculated critical thicknesses for the five quantum-well structures under study are summarized in Table 2.3. It is evident that the thickness of quantum wells used in this study is well below the critical thicknesses of the five quantum-well structures.

Table 2.3. Calculated critical thicknesses of InGaAs and InGaAlAs quantum wells with Matthews and Blakeslee model.

Quantum-well structures	Compressive strain	Critical thickness
$In_{0.02}Ga_{0.98}As$	0.143%	228.6 nm
$In_{0.08}Ga_{0.883}Al_{0.037}As$	0.575%	44.3 nm
$In_{0.14}Ga_{0.786}Al_{0.074}As$	1.004%	22.4 nm
$In_{0.20}Ga_{0.671}Al_{0.119}As$	1.497%	13.5 nm
$In_{0.26}Ga_{0.585}Al_{0.155}As$	1.848%	10.3 nm

It is also noteworthy that more indium composition in InGaAlAs quantum wells is required to increase the amount of compressive strain; however, in order to have the emission wavelength fixed at 838 nm, it is

necessary to have more aluminum composition in quantum wells when the indium composition is increased, which is not desired in view of crystal growth. Therefore, according to the simulation results, a compressive strain of approximately 1.5% in quantum wells is beneficial for the InGaAlAs/AlGaAs quantum wells for 850-nm vertical-cavity surface-emitting lasers.

2.4 Summary

The gain spectra of compressively strained $In_{0.02}Ga_{0.98}As$ and InGaAlAs quantum wells emitting at 838 nm, calculated by solving the 6×6 $k{\cdot}p$ Hamiltonian, are numerically investigated with the valence-band-mixing effect being taken into account. The simulation results suggest that, among the active layer structures under study, relatively high optical gain and differential gain, and low transparency carrier density and transparency radiative current density can be achieved by increasing the amount of compressive strain in quantum wells. However, further improvement of the optical gain and threshold properties of these quantum-well structures becomes minimal when the compressive strain in quantum wells is higher than approximately 1.5%. The simulation results also suggest that the increase of maximum differential gain with more compressive strain in quantum wells becomes less evident when the compressive strain is higher than approximately 1.5%. Therefore, a compressive strain of approximately 1.5% in InGaAlAs quantum wells is beneficial for application in high-speed 850-nm vertical-cavity surface-emitting lasers.

Chapter 3. Optimization Study of the InGaAsP Quantum-Well Structures for 850-nm VCSELs

It has been mentioned in chapter 2 that the InGaAs/AlGaAs, InGaAlAs/AlGaAs, and InGaAsP/InGaP material systems can be used as compressively strained quantum wells for 850-nm VCSELs. Although the InGaAlAs/AlGaAs can provide different strain levels in quantum wells, employing aluminum in a quantum well may cause the problem of oxidation in active region. Therefore, in this chapter, I will systematically study the alternative Al-free InGaAsP/InGaP active region for 850-nm VCSELs.

First of all, I will attempt to give an overview of the published LDs and VCSELs which utilized the strained InGaAsP/InGaP active region. Then, the optimal strain level of compressively strained InGaAsP/InGaP quantum wells will be studied systematically for 850-nm VCSELs by using the PICS3D simulation program [76].

3.1 Study Related to the Compressively Strained 850-nm InGaAsP VCSELs

The InGaAsP material system has been firmly established as a candidate for high-performance long-wavelength semiconductor lasers [94, 95]. Nevertheless, relatively few studies have been reported on Al-free InGaAsP/InGaP semiconductor lasers with an emission wavelength near 850 nm [87, 96–98]. Although the conduction band offset of the InGaAsP/InGaP heterojunction is relatively small [99, 100], the problem of electronic overflow can be overcome by using a high-bandgap layer to block the carrier leakage. Tansu *et al.* have experimentally demonstrated low-temperature sensitive InGaAsP/InGaP lasers which have higher characteristic temperature than that of GaAs/AlGaAs lasers [96].

On the other hand, tensile-strained barriers, which can provide strain compensation and reduce active region carrier leakage, can be achieved by using InGaAsP/InGaP quantum wells. High-speed oxide-confined VCSELs using InGaAsP/InGaP strain-compensated multiple-quantum wells have been demonstrated by other researchers [97]. They have reached a modulation band width of 14.5 GHz and a modulation current efficiency factor of 11.6 GHz/(mA)$^{1/2}$ [98]. Furthermore, for the strained InGaAsP/InGaP quantum wells, although the properties of strained $(Al_xGa_{1-x})_yIn_{1-y}As_zP_{1-z}$ material system was theoretically studied for 850-nm surface- and edge-emitting lasers, the amount of compressive strain

of the InGaAsP/InGaP quantum well was fixed at 1.7% [87]. To the best of our knowledge, qualitative analysis of varying compressive strain in InGaAsP quantum wells which have an emission wavelength of ~850 nm has not been well documented in literature.

3.2 Physical model and Numerical Parameters

In this paper, it is assumed that the compressively strained InGaAsP quantum wells are grown on (001)-oriented GaAs substrates. For simplicity, it is also supposed that the conduction subbands are decoupled from valence subbands and have isotropic parabolic bands, such as the situation of most III-V direct bandgap semiconductors [49]. The 6×6 Luttinger-Kohn Hamiltonian including the coupling of the heavy hole, light hole, and spin-orbit splitting bands is utilized to evaluate the nonparabolic valence band structures [48]. As for the numerical parameters required for $k{\cdot}p$ calculations for the InGaAsP materials, except for the unstrained bandgap energies, a linear interpolation between the parameters of the relevant binary semiconductors is utilized. For a physical parameter P, the interpolation formula is [88]

$$P(In_{1-x}Ga_xAs_yP_{1-y}) = P(GaAs)xy + P(GaP)x(1-y) + P(InAs)(1-x)y + P(InP)(1-x)(1-y). \tag{3.2.1}$$

The material parameters of the binary semiconductors used in this study are taken from the paper by Vurgaftman *et al.* [45] and summarized in Table 3.1. The formula for the calculation of unstrained InGaAsP bandgap energies can be expressed as a weighted sum of the bandgap energies of relevant ternary semiconductors with appropriate bowing parameters. Specifically, the unstrained InGaAsP bandgap energies are calculated by

following expressions [45]

$$E_g(InGaAsP) = \frac{x(1-x)[(1-y)E_g(GaInP) + yE_g(GaInAs)]}{x(1-x) + y(1-y)}$$

$$+ \frac{y(1-y)[xE_g(GaAsP) + (1-x)E_g(InAsP)]}{x(1-x) + y(1-y)}, \quad (3.2.2)$$

$$E_g(GaInP) = xE_g(GaP) + (1-x)E_g(InP) - x(1-x)B(GaInP), \quad (3.2.3)$$

$$E_g(GaInAs) = xE_g(GaAs) + (1-x)E_g(InAs) - x(1-x)B(GaInAs), \quad (3.2.4)$$

$$E_g(GaAsP) = yE_g(GaAs) + (1-y)E_g(GaP) - y(1-y)B(GaAsP), \quad (3.2.5)$$

$$E_g(InAsP) = yE_g(InAs) + (1-y)E_g(InP) - y(1-y)B(InAsP), \quad (3.2.6)$$

where x and y represent the compositions of gallium and arsenic in the InGaAsP material system respectively. The bandgap bowing parameters of GaInP, GaInAs, GaAsP, and InAsP are 0.65 eV, 0.477 eV, 0.19 eV, and 0.1 eV, respectively [45]. Except for GaP, the temperature dependent bandgap energies of the relevant binary semiconductors are calculated using the commonly employed Varshni formula. The values of α, β, and $E_g(T = 0)$ of the binary alloys are listed in Table 3.2 [45]. The temperature dependent bandgap energy of the GaP is calculated by the expression of 2.886 + 0.1081[1−coth(164/T)] [45]. The conduction band offset for the compressively strained InGaAsP/InGaP quantum well is set to 18% of the

total band offset [99, 100]. The optical gain spectra are also calculated by (1.2.4) and the intraband scattering time is assumed as 0.1 ps [52, 90–92] in the calculations. The spontaneous emission rate is calculated according to (1.2.9). The radiative current density J_{rad} can be calculated from (2.2.8).

Table 3.1. Material parameters of the binary semiconductors GaAs, InAs, GaP and InP.

Parameter	Symbol	GaAs	InAs	GaP	InP
Lattice constant	a_0 (Å)	5.65325	6.0583	5.4505	5.8697
Spin-orbit splitting	Δ_{so} (eV)	0.341	0.39	0.08	0.108
Luttinger parameter	γ_1	6.98	20.0	4.05	5.08
	γ_2	2.06	8.5	0.49	1.6
	γ_3	2.93	9.2	2.93	2.1
Hydrost. deform. potential	a (eV)	–8.33	–6.08	–9.9	–6.6
Shear deform. potential	b (eV)	–2.0	–1.8	–1.6	–2.0
Elastic constant	C_{11} (GPa)	1221	832.9	1405	1011
Elastic constant	C_{12} (GPa)	566	452.6	620.3	561
Electron eff. mass	m_e/m_o	0.067	0.026	0.13	0.0795

Table 3.2. Varshni parameters of the binary semiconductors GaAs, InAs, and InP.

Parameter (unit)	GaAs	InP	InAs
α (meV/K)	0.5405	0.363	0.276
β (K)	204	162	93
E_g ($T = 0$) (eV)	1.519	1.4236	0.417

3.3 Simulation Result and Discussion

In this study, in order to obtain the optimal InGaAsP/InGaP quantum-well structure for 850-nm VCSELs, the optical gain and threshold properties of compressively strained InGaAsP/InGaP quantum wells emitting at 840 nm with different strains are investigated using 6×6 *k·p* Hamiltonian including the heavy hole, light hole, and spin-orbit splitting bands. A gain-cavity detuning of approximately 10 nm is usually introduced for the design of 850-nm VCSELs to result in a flat threshold current versus temperature behavior over some range of temperature operation. Based on the 6×6 *k·p* theory, the optical gain spectra, transparency carrier densities, transparency radiative current densities, and maximum differential gain for the InGaAsP quantum wells with different compressive strains are compared and discussed.

To study the effects of compressive strains on the properties of the 840-nm InGaAsP quantum wells, five quantum-well structures including $In_{0.02}Ga_{0.98}As_{0.981}P_{0.019}$, $In_{0.12}Ga_{0.88}As_{0.892}P_{0.108}$, $In_{0.22}Ga_{0.78}As_{0.799}P_{0.201}$, $In_{0.32}Ga_{0.68}As_{0.704}P_{0.296}$, and $In_{0.42}Ga_{0.58}As_{0.607}P_{0.393}$ are systematically studied in this chapter, which have corresponding in-plane compressive strains of 0.075%, 0.473%, 0.859%, 1.239%, and 1.615%, respectively. All of the quantum wells have the same thickness of 8 nm and the same barrier layer of $In_{0.4}Ga_{0.6}P$. Since the indium composition dominates the amount of compressive strain, the indium composition is varied with a fixed step of

10% and the appropriate phosphor composition is chosen in such a way that the emission wavelength of the quantum-well structures resulted from transitions between the lowest conduction subband (C1) and the top valence subband (HH1) is 840 nm.

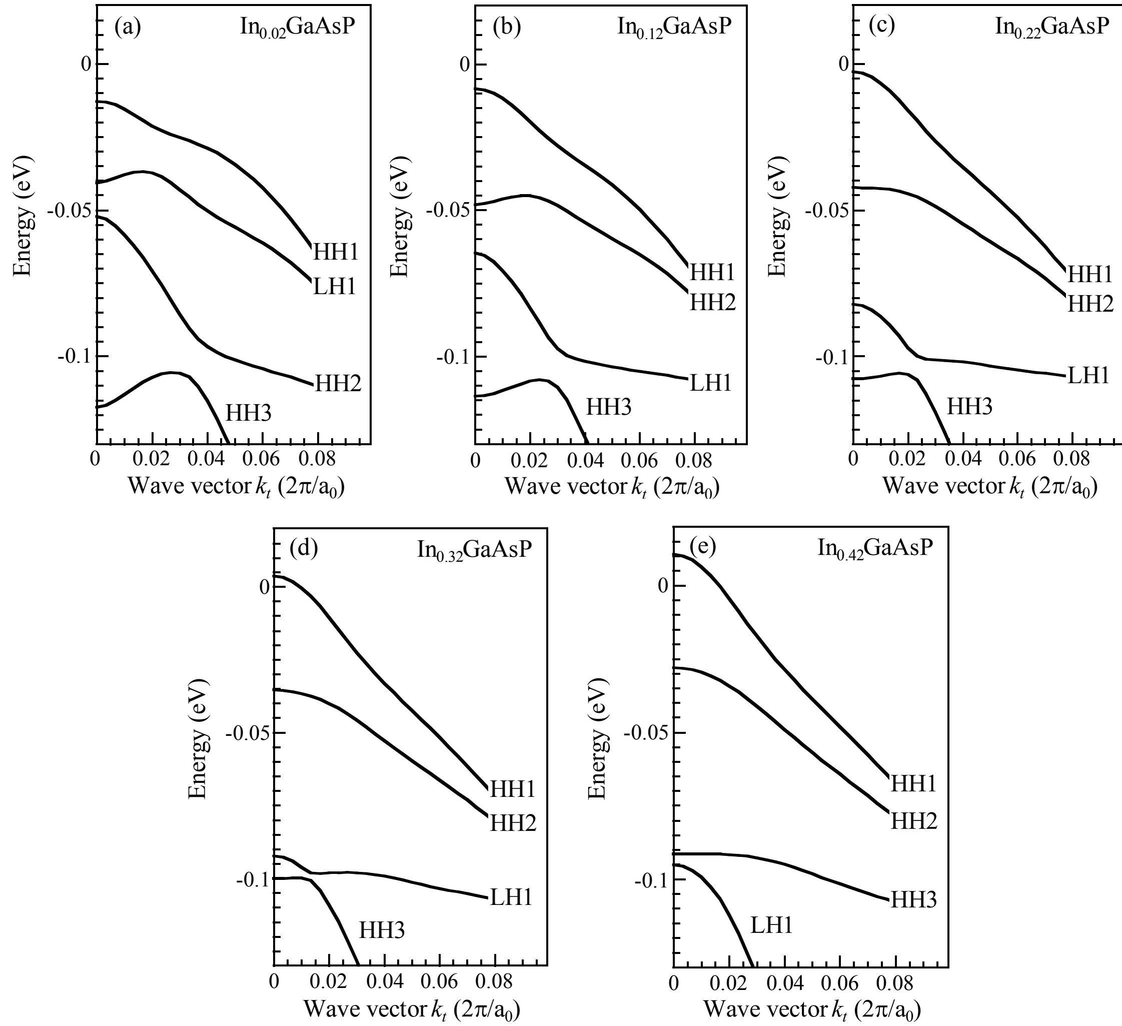

Fig. 3.1. Valence subband structures for 8-nm InGaAsP quantum well sandwiched between $In_{0.4}Ga_{0.6}P$ barriers for (a) $In_{0.02}Ga_{0.98}As_{0.981}P_{0.019}$, (b) $In_{0.12}Ga_{0.88}As_{0.892}P_{0.108}$, (c) $In_{0.22}Ga_{0.78}As_{0.799}P_{0.201}$, (d) $In_{0.32}Ga_{0.68}As_{0.704}P_{0.296}$, and (e) $In_{0.42}Ga_{0.58}As_{0.607}P_{0.393}$.

Figures 3.1(a)–3.1(e) show the valence subband structures for the compressively strained InGaAsP/InGaP quantum wells with variant indium and arsenic compositions as a function of the in-plane wave vector k_t, which is along the horizontal axis and normalized by $2\pi/a_0$. It is worthy to mention that only four valence subbands near the band edge are shown in Fig. 3.1 because the lower energy subbands dominate the threshold properties and differential gain of the quantum wells. According to these valence-band dispersion curves, the top valence bands are heavy hole subbands in nature due to the compressive strain. In the case of Fig. 3.1(a), the significantly non-parabolic valence subbands observed in the subband structure are the direct result of the band mixing between HH1 and LH1 subbands. When the compressive strain increases with more indium composition in the quantum well, the strain separates the HH1 and LH1 subbands, pushing the LH1 subband away from the HH1. As a result, the valence-band-mixing effects are greatly reduced and the degree of band warping of HH1 is increased due to the increase of compressive strain in the quantum wells. Under this circumstance, the effective mass of the holes becomes lighter, which makes the density of states in valence and conduction bands more matched. This condition is expected to result in a much higher differential gain and lower transparency carrier density simultaneously. On the other hand, the distance of separation between LH1 and HH1 subbands increases with compressive strain in the quantum wells, which will reduce the component of TM mode in optical gain.

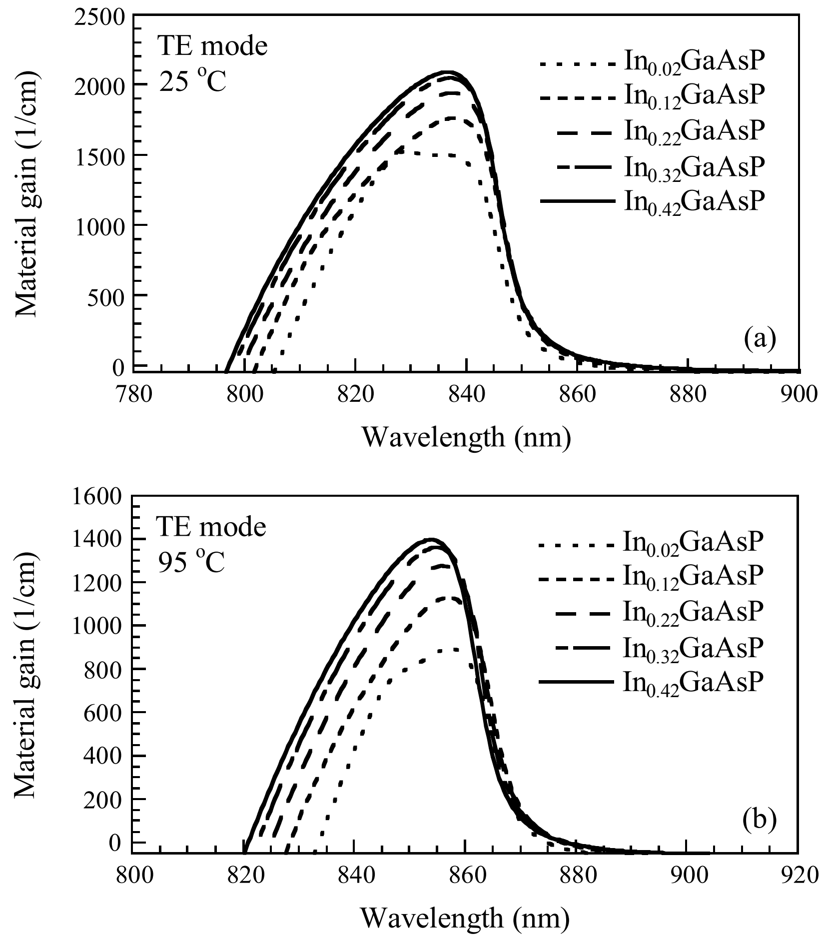

Fig. 3.2. Gain spectra of compressively strained InGaAsP/InGaP quantum wells at (a) 25 °C and (b) 95 °C.

Figure 3.2 shows the optical gain spectra of the InGaAsP quantum wells at a fixed carrier density 5×10^{18} cm^{-3} for TE mode at 25 °C and 95 °C. Since the cases of the InGaAsP quantum wells under study are subject to compressive strain, we solely compare the TE mode of different quantum-well structures because the TM mode is strongly depressed with high compressive strain in quantum wells. Besides, the TM mode is mainly introduced by C1-LH1 transition which provides shorter emitting

wavelength than 840 nm. Comparing Fig. 3.1 (a) with Fig. 3.2 (a), there is a second peak in the gain spectrum of the $In_{0.02}Ga_{0.98}As_{0.981}P_{0.019}$ quantum well due to the smaller separation distance between HH1 and LH1 [see Fig. 3.1 (a)]. Thus, a portion of the injected carriers will be consumed in the C1-LH1 transitions. On the contrary, the separation distance between HH1 and LH1 increases with compressive strain. This situation leaves more carriers for the C1-HH1 transitions so that the peak gain for TE mode is higher with more compressive strain in the quantum wells. However, it is noteworthy that, further increase in material gain becomes minimal when the compressive strain is higher than approximately 1.24%. Furthermore, comparing Fig. 3.2 (a) with Fig. 3.2 (b), the gain peak does not vary obviously with temperature when the compressive strain increases. This is beneficial for VCSELs since fast gain shift is a main reason of degradation for VCSELs operating at high temperature due to the spectral misalignment between the cavity mode and the gain spectrum.

Figure 3.3 depicts the peak material gain of TE mode as a function of carrier density for InGaAsP quantum wells at 25 °C and 95 °C. When the compressive strain increases, the transparency carrier density decreases. This is attributed to the higher valence band curvature in the compressively strained quantum well resulting in smaller joint densities of states. In this condition, the creation of population inversion can be easily achieved [93]. Moreover, the peak material gain increases with the compressive strain in quantum wells. As shown in Fig. 3.3 (b), similar trend is observed when the

temperature is 95 °C.

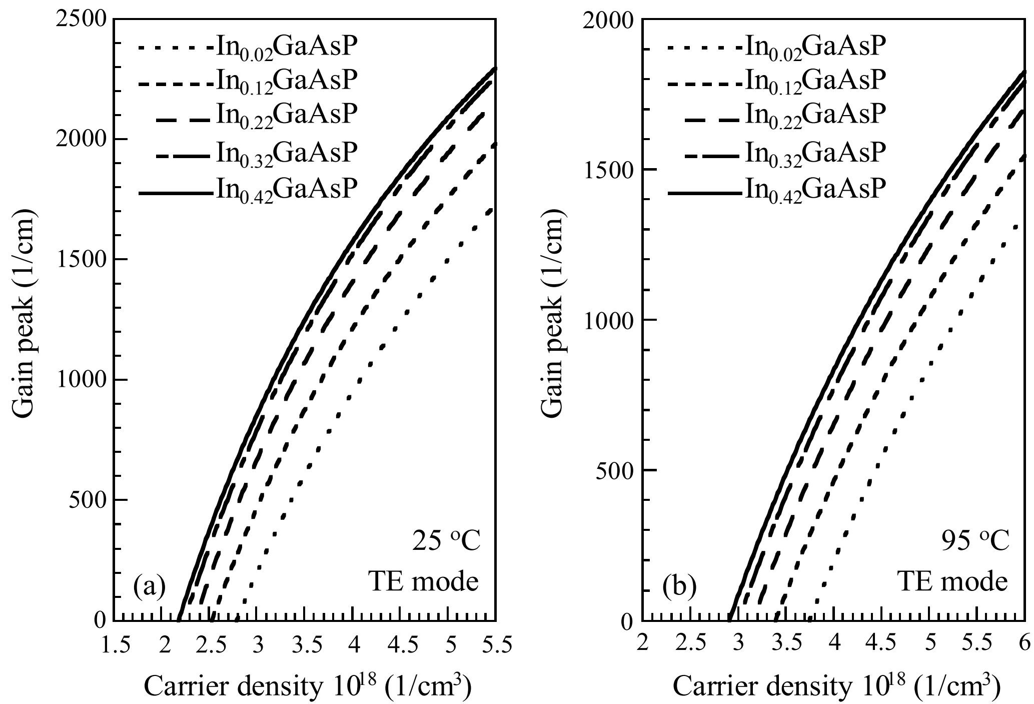

Fig. 3.3. Peak material gain of TE mode as a function of carrier density for InGaAsP/InGaP quantum wells at (a) 25 °C and (b) 95 °C.

Figure 3.4 shows the peak material gain of TE mode as a function of radiative current density for InGaAsP/InGaP quantum wells at 25 °C and 95 °C. The transparency radiative current density becomes lower when the composition of indium in quantum wells increases. It can be concluded according to Figs. 3.3 and 3.4 that, higher compressive strain in quantum wells results in lower transparency carrier density and transparency radiative current density and higher peak material gain. Nevertheless, it should be mentioned that, the peak material gain in the range of carrier density and radiative current density under study does not have evident

change when the amount of the compressive strain is higher than approximately 1.24%.

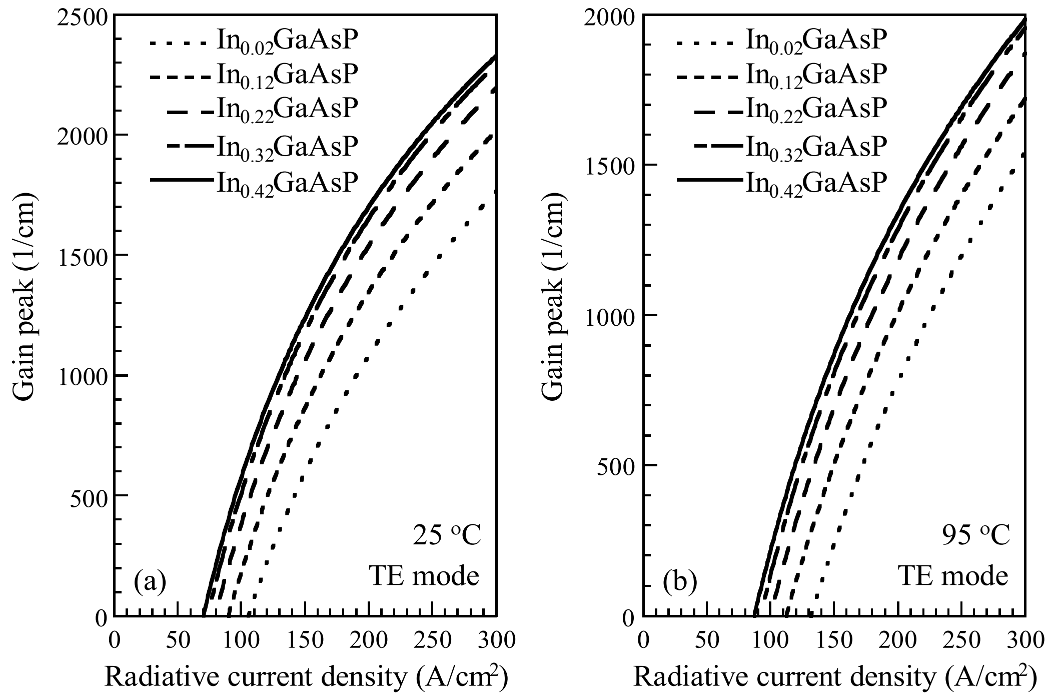

Fig. 3.4. Peak material gain of TE mode as a function of radiative current density for InGaAsP/InGaP quantum wells at (a) 25 °C and (b) 95 °C.

For convenient comparison among the properties of InGaAsP quantum wells with different compressive strains, the transparency carrier densities and transparency radiative current densities at 25 °C and 95 °C are depicted as a function of the compressive strain in InGaAsP quantum wells in Fig. 3.5. The decrease of transparency carrier density and transparency radiative current density with an increase in compressive strain at 25 °C and 95 °C becomes less apparent when the compressive strain in quantum wells is larger than about 1.24%. This can be explained with the valence subband

structures of InGaAsP quantum wells, as shown in Fig. 3.1. The band curvature of the HH1 subband, which dominates the transition in the case of compressively strained quantum wells, does not change evidently when the compressive strain is larger than ~1.24%. It means that the density of states near the top of valence band does not change obviously when the compressive strain in quantum wells is higher than ~1.24%.

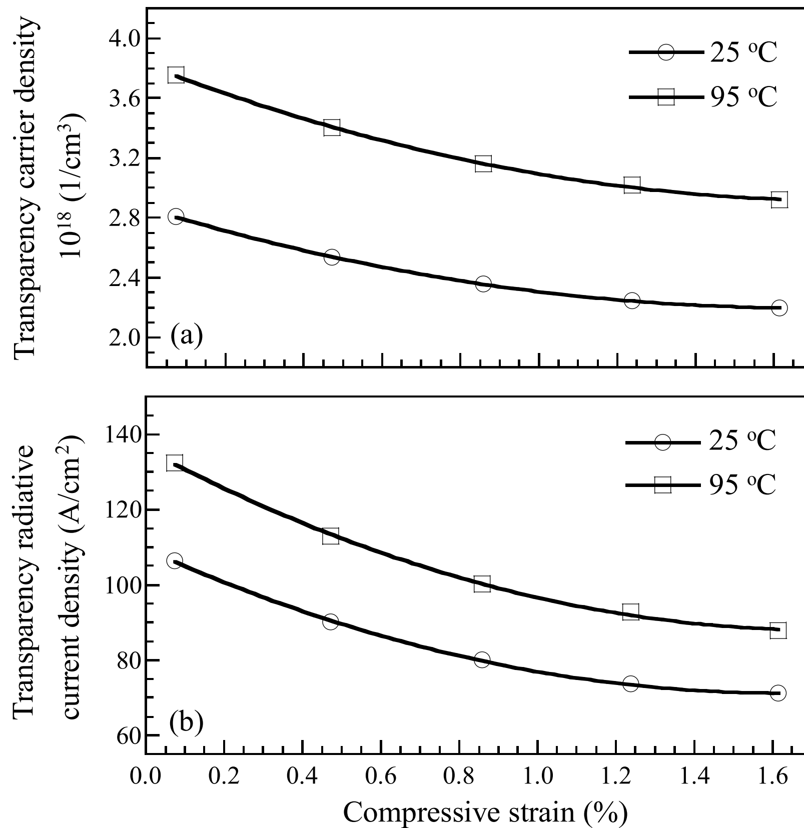

Fig. 3.5. (a) Transparency carrier density and (b) transparency radiative current density of TE mode as a function of compressive strain at 25 °C and 95 °C.

Moreover, since the transparency carrier density is primarily decided by the Bernard-Duraffourg inversion condition which requires that the

separation between quasi-Fermi levels be greater than the bandgap, the value of $(F_c - F_v)$ is sensitive to the density of states near the top of the valence band when the carriers are injected into the quantum wells. Therefore, the characteristics of the InGaAsP quantum wells under study do not vary markedly when the compressive strain in quantum wells is higher than approximately 1.24%.

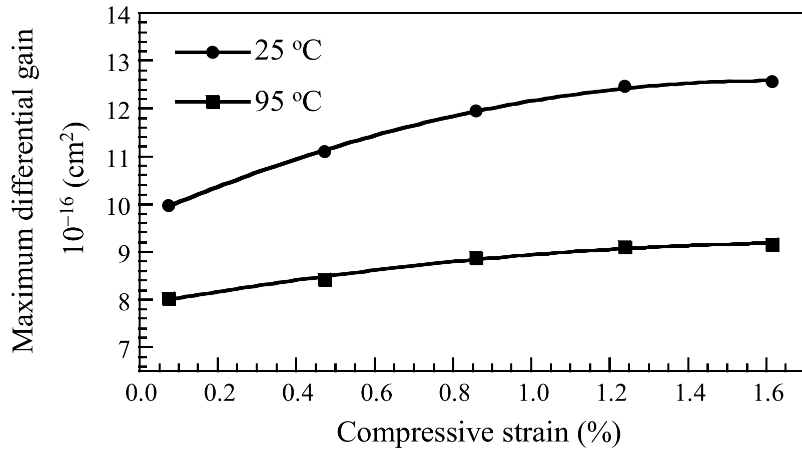

Fig. 3.6. Maximum differential gain of TE mode as a function of compressive strain at 25 °C and 95 °C.

To discuss the high-speed properties, the calculated values of the maximum differential gain are plotted as a function of the compressive strain in quantum wells at 25 °C and 95 °C in Fig. 3.6. Evidently, the maximum differential gain increases with the compressive strain in quantum wells. It is attractive that the increase of maximum differential gain with more compressive strain in quantum wells becomes less evident when the compressive strain is higher than approximately 1.24% as well. Consequently, the variation of valence subband structures with the amount

of compressive strain in quantum wells still plays an important role for the differential gain of InGaAsP quantum wells.

Table 3.3. Calculated critical thicknesses of InGaAsP quantum wells with Matthews and Blakeslee model.

Quantum-well structures	Compressive strain	Critical thickness
$In_{0.02}Ga_{0.98}As_{0.981}P_{0.019}$	0.075%	478.7 nm
$In_{0.12}Ga_{0.88}As_{0.892}P_{0.108}$	0.473%	55.9 nm
$In_{0.22}Ga_{0.78}As_{0.799}P_{0.201}$	0.859%	27.1 nm
$In_{0.32}Ga_{0.68}As_{0.704}P_{0.296}$	1.239%	17.1 nm
$In_{0.42}Ga_{0.58}As_{0.607}P_{0.393}$	1.615%	12.2 nm

It should be mentioned here that, although the optical properties of compressively strained InGaAsP quantum wells can be improved by introducing larger amount of compressive strain in quantum wells, the amount of strain in quantum wells will be limited by the critical thickness for practical crystal growth. Therefore, in order to estimate the critical thicknesses of the five InGaAsP/InGaP quantum-well structures under study, the Matthews and Blakeslee model [56], which has been used to evaluate the critical thickness of many material systems [65−68], is utilized. In the calculations, the lattice constants and elastic constants are taken from Table 3.1. The calculated values of the critical thicknesses for the five quantum-well structures under study are tabulated in Table 3.3. It is evident that the thickness of quantum wells used in this study is well below the critical thicknesses of the five quantum-well structures. Therefore,

according to the simulation results, a compressive strain of approximately 1.24% in quantum wells is beneficial for the InGaAsP/InGaP quantum wells for 850-nm vertical-cavity surface-emitting lasers.

3.4 Summary

We have investigated the properties of the compressively strained InGaAsP quantum-well structures emitting at 840 nm by solving the 6×6 $k{\cdot}p$ Hamiltonian. The simulation results indicate that, among the active layer structures under study, relatively high optical gain and differential gain, and low transparency carrier density and transparency radiative current density can be achieved by increasing the amount of compressive strain in quantum wells. However, further improvement of the optical gain and threshold properties of the quantum-well structures becomes minimal when the compressive strain in quantum wells is higher than approximately 1.24%. Therefore, a compressive strain of approximately 1.24% in InGaAsP quantum wells is beneficial for application in high-speed 850-nm vertical-cavity surface-emitting lasers.

Chapter 4. Conclusion

In this thesis, the properties of compressively strained quantum-well structures with an emission wavelength near 850 nm are theoretically investigated for 850-nm vertical-cavity surface-emitting lasers by solving the 6×6 *k·p* Hamiltonian. Specifically, the compressively strained material systems including InGaAs, InGaAlAs, and InGaAsP are discussed in an attempt to obtain optimal strain level in the quantum wells. For InGaAlAs/AlGaAs material system, five quantum-well structures including $In_{0.02}Ga_{0.98}As$, $In_{0.08}Ga_{0.883}Al_{0.037}As$, $In_{0.14}Ga_{0.786}Al_{0.074}As$, $In_{0.20}Ga_{0.671}Al_{0.119}As$, and $In_{0.26}Ga_{0.585}Al_{0.155}As$ are studied, which have corresponding in-plane compressive strains of 0.143%, 0.575%, 1.004%, 1.497%, and 1.848%, respectively. The simulation results suggest that the maximum optical gain, transparency carrier densities, transparency radiative current densities, and differential gain of InGaAlAs quantum wells can be improved by employing more compressive strain in quantum wells. Nevertheless, further improvement of the optical and threshold properties of InGaAlAs quantum wells becomes minimal when the compressive strain is higher than approximately 1.5%.

In the case of InGaAsP/InGaP material system, the quantum-well structures including $In_{0.02}Ga_{0.98}As_{0.981}P_{0.019}$, $In_{0.12}Ga_{0.88}As_{0.892}P_{0.108}$, $In_{0.22}Ga_{0.78}As_{0.799}P_{0.201}$, $In_{0.32}Ga_{0.68}As_{0.704}P_{0.296}$, and $In_{0.42}Ga_{0.58}As_{0.607}P_{0.393}$ are discussed, which have corresponding in-plane compressive strains of

0.075%, 0.473%, 0.859%, 1.239%, and 1.615%, respectively. According to the simulation results, it can be found that relatively high optical gain and differential gain, and low transparency carrier density and transparency radiative current density can be obtained by increasing the amount of compressive strain in quantum wells. However, it is noteworthy that further improvement of the optical gain and threshold properties of the InGaAsP/InGaP quantum-well structures becomes minimal when the compressive strain is higher than approximately 1.24%. Therefore, the optimal compressive strains are approximately 1.24% and 1.5% for InGaAsP and InGaAlAs quantum wells, respectively. Both material systems are beneficial for application in high-speed 850-nm vertical-cavity surface-emitting lasers.

The numerical simulation results obtained in this thesis may be used as references for the design of compressively strained 850-nm vertical-cavity surface-emitting lasers.

References

[1] C. Wilmsen, H. Temkin, and L. A. Coldren, Eds., "*Vertical-Cavity Surface-Emitting Lasers: Design, Fabrication, Characterization, and Applications*," Cambridge Studies in Modern Optics, Cambrideg University Press, New York, 1999.

[2] M. I. Nathan, W. P. Dumke, G. Burns, F. H. Dill Jr., and G. Lasher, "Stimulated emission of radiation from GaAs p-n junctions," *Appl. Phys. Lett.*, vol. 1, pp. 62–64, 1962.

[3] R. N. Hall, G. H. Fenner, J. D. Kingsley, T. J. Soltys, and R. D. Carlson, "Coherent light emission from GaAs junctions," *Phys. Rev. Lett.*, vol. 9, pp. 366–368, 1962.

[4] T. M. Quist, R. H. Rediker, R. J. Keyes, W. E. Krag, B. Lax, A. L. McWhorter, and H. J. Zeiger, "Semiconductor maser of GaAs," *Appl. Phys. Lett.*, vol. 1, pp. 91–92, 1962.

[5] N. Holonyak Jr. and S. Bevacqua, "Coherent (visible) light emission From $Ga(As_{1-x}P_x)$ junctions," *Appl. Phys. Lett.*, vol. 1, pp. 82–83, 1962.

[6] I. Hiyashi, M. B. Panish, and P. W. Foy, "A technique for the preparation of low-threshold room-temperature GaAs laser diode structures," IEEE J. Quantum Electron., vol. 5, pp. 210–212, 1969.

[7] H. Soda, K. Iga, C. Kitahara, and Y. Suematsu, "GaInAsP/InP surface emitting injection lasers," *Jpn. J. Appl. Phys.*, vol. 18, pp. 2329–2330, 1979.

[8] M. Ogura, W. Hsin, M.-C. Wu, S. Wang, J. R. Whinnery, S. C. Wang, and J. J. Yang, "Surface-emitting laser diode with vertical GaAs/GaAlAs quarter-wavelength multilayer and lateral buried heterostructure," *Appl. Phys. Lett.*, vol. 51, pp. 1655–1657, 1987.

[9] Y. H. Lee, J. L. Jewell, A. Scherer, S. L. Mc. Call, J. P. Harbison, and L. T. Florez, "Room-temperature continuous-wave vertical cavity

single-quantum-well microlaser diodes," *Electron. Lett.*, vol. 25, pp. 1377–1378, 1989.

[10] A. Sherer, J. L. Jeell, Y. H. Lee, J. P. Harbison, and L. T. Florez, "Fabrication of microlasers and microresonato optical switches," *Appl. Phys. Lett.*, vol. 55, pp. 2724–2726, 1989.

[11] R. S. Geels, S. W. Corzine, J. W. Scott, D. B. Young, and L. A. Coldren, "Low threshold planarized vertical-cavity surface-emitting lasers," *IEEE Photon. Technol. Lett.*, vol. 2, pp. 234–236, 1990.

[12] K. D. Choquette, G. Hasnain, Y. H. Wang, J. D. Wynn, R. S. Freund, A. Y. Cho, and R. E. Leibenguth, "GaAs vertical-cavity surface-emitting lasers fabricated by reactive ion etching," *IEEE Photon. Technol. Lett.*, vol. 3, pp. 859–862, 1991.

[13] B. J. Thibeault, T. A. Strand, T. Wipiejewski, M. G. Peters, D. B. Young, S. W. Corzine, L. A. Coldren, and J. W. Scott, "Evaluating the effects of optical and carrier osses in etched-post vertical cavity lasers," *J. Appl. Phys.*, vol. 78, pp. 5871–5875, 1995.

[14] C. J. Chang-Hasnain, M. Orenstein, A. Vonlehmen, L. T. Florez, J. P. Harbison, and N. G. Stoffel, "Transverse mode characteristics of vertical cavity surface-emitting lasers," *Appl. Phys. Lett.*, vol. 57, pp. 218–220, 1990.

[15] G. Hasnain, K. Tai, L. Yang, Y. H. Wang, R. J. Fischer, J. D. Wynn, B. Weir, N. K. Dutta, and A. Y. Cho, "Performance of gain-guided surface emitting lasers with semiconductor distributed Bragg reflectors," *IEEE J. Quantum Electron.*, vol. 27, pp. 1377–1385, 1991.

[16] G. R. Hadley, K. L. Lear, M. E. Warren, K. D. Choquette, J. W. Scott, and S. W. Corzine, "Comprehensive numerical modeling of vertical-cavity surface-emitting lasers," *IEEE J. Quantum Electron.*, vol. 32, pp. 607–616, 1996.

[17] D. Vakhshoori, J. D. Wynn, G. J. Aydzik, R. E. Leibengnth, M. T.

Asom, K. Kojima, and R. A. Morgan, "Top-surface emitting lasers with 1.9 V threshold voltage and the effect of spatial hole burning on their transverse mode operation and efficiencies," *Appl. Phys. Lett.*, vol. 62, pp. 1448–1450, 1993.

[18] K. D. Choquette, R. P. Schneider, Jr., K. L. Lear, and K. M. Geib, "Low threshold voltage vertical-cavity lasers fabricated by selective oxidation," *Electron. Lett.*, vol. 30, pp. 2043-2044, 1994.

[19] K. D. Choquette, K. M. Geib, C. I. H. Ashby, R. D. Twesten, O. Blum, H. Q. Hou, D. M. Follstaedt, B. E. Hammons, D. Mathes, and R. Hull, "Advances in selective wet oxidation of AlGaAs alloys," *IEEE J. Select. Topics Quantum Electron.*, vol. 3, pp. 916-926, 1997.

[20] K. D. Choquette, K. L. Lear, R. P. Schneider, Jr., and K. M. Geib, "Cavity characteristics of selectively oxidized vertical-cavity lasers," *Appl. Phys. Lett.*, vol. 66, pp. 3413–3415, 1995.

[21] A. E. Bond, P. D. Dapkus, and J. D. O'Brien, "Aperture placement effects in oxide-defined vertical-cavity surface-emitting lasers," *IEEE Photon. Technol. Lett.*, vol. 10, pp. 1362–1364, 1998.

[22] A. E. Bond, P. D. Dapkus, and J. D. O'Brien, "Aperture dependent loss analysis in vertical-cavity surface-emitting lasers," *IEEE Photon. Technol. Lett.*, vol. 11, pp. 379–399, 1999.

[23] R. Pu, C. W. Wilmsen, K. M. Geib, and K. D. Choquette, "Thermal resistance of VCSEL's bonded to integraed circuits," *IEEE Photon. Technol. Lett.*, vol. 11, pp. 1554–1556, 1999.

[24] M. H. MacDougal, P. D. Dapkus, A. E. Bond, C.-K. Lin, and J. Geske, "Design and fabrication of VCSEL's with Al_xO_y–GaAs DBR's," *IEEE J. Select. Topics Quantum Electron.*, vol. 3, pp. 905-915, 1997.

[25] Y. H. Lo, R. Bhat, D. M. Hwang, C. Chua, and C. H. Lin, "Semiconductor lasers on Si substrates using the technology of bonding by atomic rearrangement," *Appl. Phys. Lett.*, vol. 62, pp. 1038–1040, 1993.

[26] S. L. Chuang, "*Physics of Optoelectronic Devices*," Wiley, New York, 1995.

[27] E. F. Schubert, Y.-H. Wang, A. Y. Cho, L.-W. Tu, and G. J. Zydzik, "Resonant cavity light-emitting diode," *Appl. Phys. Lett.*, vol. 60, pp. 921–923, 1992.

[28] K. Tai, L. Yang, Y. H. Wang, J. D. Wynn, and A. Y. Cho, "Drastic reduction of series resistance in doped semiconductor distributed Bragg reflectors for surface-emitting lasers," *Appl. Phys. Lett.*, vol. 56, pp. 2496–2498, 1990.

[29] M. G. Peters, B. J. Thibeault, D. B. Young, J. W. Scott, F. H. Peters, A. C. Gossard, and L. A. Coldren, "Band-gap engineered digital alloy interfaces for lower resistance vertical-caviy surface-emitting lasers," *Appl. Phys. Lett.*, vol. 63, pp. 3411–3413, 1993.

[30] J. M. Fastenau and G. Y. Robinson, "Low-resistance visibl wavelength distribute Bragg reflectors using small energy band offset heterojunctions," *Appl. Phys. Lett.*, vol. 74, pp. 3758–3760, 1999.

[31] M. Sugimoto, H. Kosaka, K. Kurihara, I. Ogura, T. Numai, and K. Kasahara, "Very low threshold current densit in vertical-cavity surface-emittinglaser diodes with periodically doped distributed Bargg reflectors," *Electron. Lett.*, vol. 28, pp. 385–387, 1992.

[32] G. Hasnain, K. Tai, L. Yang, Y. H. Wang, R. J. Fischer, J. D. Wynn, B. Weir, N. K. Dutta, and A. Y. Cho, "Performance of gain-guided surface emitting lasers with semiconductor distriuted Bragg reflectors," *IEEE J. Quantum Electron.*, vol. 27, pp. 1377–1385, 1991.

[33] K. D. Choquette and H. Q. Hou, "Vertical-caivty surface emitting lasers: Moving from research to manufacturing," *Proc. IEEE*, vol. 85, pp. 1730–1739, 1997.

[34] D. B. Young, J. W. Scott, F. H. Peters, M. G. Peters, M. L. Majewski, B. J. Thibeault, S. W. Corzine, and L. A. Coldren, "Enhanced

performance of offset-gain high-barrier vertical-caivty surface-emitting lasers," *IEEE J. Quantum Electron.*, vol. 29, pp. 2013–2021, 1993.

[35] A. Cho, "Film deposition by molecular beam techniques," *J. Vac. Sci. Tech.*, vol. 8, pp. S31–S38, 1971.

[36] P. L. Gourley and T. J. Drummond, "Single crystal, epitaxial multilayers of AlAs, GaAs, and $Al_xGa_{1-x}As$ for use as optical interferometric elements," *Appl. Phys. Lett.*, vol. 49, pp. 489–491, 1986.

[37] J. L. Jewell, Y. H. Lee, S. L. McCall, J. P. Harbison, and L. T. Florez, "High-finesse (Al,Ga)As interference filters grown by molecular beam epitaxy," *Appl. Phys. Lett.*, vol. 53, pp. 640–642, 1988.

[38] M. J. Ludowise, "Metalorganic chemical vapor deposition of III-V semiconductors," *J. App. Phys.*, vol. 58, pp. R31–R55, 1984.

[39] T. E. Sale, "Vertical Cavity Surface Emitting Lasers," Wiley, New York, 1995.

[40] R. S. Geels, S. W. Corzine, and L. A. Coldren, "InGaAs vertical-cavity surface-emitting lasers," *IEEE J. Quantum Electron.*, vol. 27, pp. 1359–1367, 1991.

[41] R. S. Geels, S. W. Corzine, J. W. Scott, D. B. Young, and L. A. Coldren, "Low threshold planarized vertical-cavity surface-emitting lasers," *IEEE Photon. Technol. Lett.*, vol. 2, pp. 234–236, 1990.

[42] P. Zhou, J. Cheng, C. F. Schaus, S. Z. Sun, K. Zheng, E. Armour, C. Hains, W. Hsin, D. R. Myers, and G. A. Vawter, "Low series resistance high-efficiency GaAs/AlGaAs vertical-cavity surface-emitting lasers with continuously graded mirrors grown by MOCVD," *IEEE Photon. Technol. Lett.*, vol. 3, pp. 591–593, 1991.

[43] H. Q. Hou, H. C. Chui, K. D. Choquette, B. E. Hammons, W. G. Breiland, and K. M. Geib, "Highly uniform and reproducible vertical-cavity surface-emitting lasers grown by metalorganic vapor

phase epitaxy with in situ reflectometry," *IEEE Photon. Technol. Lett.*, vol. 8, pp. 1285–1287, 1996.

[44] W. G. Breiland and K. P. Killeen, "A virtual interface method for extracting growth rates and high temperature optical constants from thin films using *in suit* normal incidence reflectance," *J. Appl. Phys.*, vol. 78, pp. 6726–6731, 1995.

[45] I. Vurgaftman, J. R. Meyer, and L. R. Ram-Mohan, "Band parameters for III–V compound semiconductors and their alloys," *J. Appl. Phys.*, vol. 89, pp. 5815–5875, 2001.

[46] J. M. Luttinger and W. Kohn, "Motion of electrons and holes in perturbed periodic fields," *Phys. Rev.*, vol. 97, pp. 869–883, 1955.

[47] J. M. Luttinger, "Quantum theory of cyclotron resonance in semiconductors: general theory," *Phys. Rev.*, vol. 102, pp. 1030–1041, 1956.

[48] C. Y. P. Chao and S. L. Chuang, "Spin-orbit-coupling effects on the valence-band structure of strained semiconductor quantum wells," *Phys. Rev. B*, vol. 46, pp. 4110–4122, 1992.

[49] C.-S. Chang and S. L. Chuang, "Modeling of strained quantum-well lasers with spin-orbit coupling," *IEEE J. Select. Topics Quantum Electron.*, vol. 1, pp. 218–229, 1995.

[50] S. L. Chuang and C. S. Chang, "A band-structure model of strained quantum-well wurtzite semiconductors," *Semicond. Sci. Technol.*, vol. 12, pp. 252–263, 1997.

[51] S. Colak, R. Eppenga, and M. F. H. Schuurmans, "Band mixing effects on quantum well gain," *IEEE J. Quantum Electron.*, vol. 23, pp. 960–967, 1987.

[52] D. Ahn, S. L. Chuang, Y.-C. Chang, "Valence-band mixing effects on the gain and the refractive index change of quantum-well lasers," *J. Appl. Phys.*, vol. 64, pp. 4056–4064, 1988.

[53] E. Yablonovitch and E. O. Kane, "Reduction of lasing threshold

current density by the lowering of valence band effective mass," *J. Lightwave Technol.*, vol. 4, pp. 504–506, 1986.

[54] E. P. O'Reilly and A. R. Adams, "Band-structure engineering in strained semiconductor lasers," *IEEE J. Quantum Electron.*, vol. 30, pp. 366–379, 1994.

[55] S. W. Corzine, R. H. Yan, and L. A. Coldren, "Theoretical gain in strained InGaAs/AlGaAs quantum wells including valence-band mixing effects," *Appl. Phys. Lett.*, vol. 57, pp. 2835–2837, 1990.

[56] J. W. Matthews and A. E. Blakeslee, "Defects in epitaxial multilayers: I. Misfit dislocations," *J. Crystal Growth*, vol. 27, pp. 118–125, 1974.

[57] J. W. Matthews, S. Mader, and T. B. Light, "Accommodation of misfit across the interface between crystals of semiconducting elements or compounds," *J. Appl. Phys.*, vol. 41, pp. 3800–3804, 1970.

[58] P. S. Zory, Ed., "Quantum Well Lasers," Academic Press, San Diego, California, USA, 1993.

[59] R. People and J. C. Bean, "Calculation of critical layer thickness versus lattice mismatch for Ge_xSi_{1-x}/Si strained-layer heterostructures," *Appl. Phys. Lett.*, vol. 47, pp. 322–324, 1985.

[60] R. People and J. C. Bean, "Erratum: Calculation of critical layer thickness versus lattice mismatch for Ge_xSi_{1-x}/Si strained layer heterostructures," *Appl. Phys. Lett.*, vol. 49, pp. 229–229, 1986.

[61] I. J. Fritz, S. T. Picraux, L. R. Dawson, T. J. Drummond, W. D. Laidig, and N. G. Anderson, "Dependence of critical layer thickness on strain for $In_xGa_{1-x}As$/GaAs strained-layer superlattices," *Appl. Phys. Lett.*, vol. 46, pp. 967–969, 1985.

[62] T. G. Andersson, Z. G. Chen, V. D. Kulakovskii, A. Uddin, and J. T. Vallin, "Variation of the critical layer thickness with In content in strained $In_xGa_{1-x}As$-GaAs quantum wells grown by molecular beam epitaxy," *Appl. Phys. Lett.*, vol. 51, pp. 752–754, 1987.

[63] J. Y. Yao, T. G. Andersson, and G. L. Dunlop, "Structure of

lattice-strained $In_xGa_{1-x}As/GaAs$ layers studied by transmission electron microscopy," *Appl. Phys. Lett.*, vol. 53, pp. 1420–1422, 1988.

[64] S.-L. Weng, "Experimental studies of misfit dependence of critical layer thickness in pseudomorphic InGaAs single-strained quantum-well structures," *J. Appl. Phys.*, vol. 66, pp. 2217–2219, 1989.

[65] X. Wu, J.-M. Baribeau, J. A. Gupta, and M. Beaulieu, "Strain relaxation in GaN_yAs_{1-y} films on (100) GaAs," *J. Crystal Growth*, vol. 282, pp. 18–28, 2005.

[66] Y.-C. Liang, H.-Y. Lee, H.-J. Liu, C.-K. Huang, and T.-B. Wu, "Real-time X-ray study of roughness scaling in the initial growth of epitaxial $BaTiO_3/LaNiO_3$ superlattices," *J. Crystal Growth*, vol. 279, pp. 114–121, 2005.

[67] T. Kitatani, A. Taike, and M. Aoki, "Strain relaxation in InGaAsP/InP grown by metal-organic vapor-phase epitaxy," *J. Crystal Growth*, vol. 273, pp. 19–25, 2004.

[68] H. C. Kuo, H. H. Yao, Y. H. Chang, Y. A. Chang, M. Y. Tsai, J. Hsieh, E. Y. Chang, and S. C. Wang, "MOCVD growth of highly strained InGaAs:Sb–GaAs–GaAsP quantum well vertical cavity surface-emitting lasers with 1.27 μm emission," *J. Crystal Growth*, vol. 272, pp. 538–542, 2004.

[69] K. Iga, "Surface-emitting laser–Its birth and generation of new optoelectronics field," *IEEE J. Select. Topics Quantum Electron.*, vol. 6, pp. 1201–1215, 2000.

[70] W. W. Chow, K. D. Choquette, M. H. Crawford, K. L. Lear, and G. R. Hadley, "Design, fabrication, and performance of infrared and viible vertical-cavity surface-emitting lasers," *IEEE J. Quantum Electron.*, vol. 33, pp. 1810–1824, 1997.

[71] G. Sialm, D. Lenz, D. Erni, G.-L. Bona, C. Kromer, M. X. Jungo, T.

Morf, F. Ellinger, and H. Jäckel, "Comparison of simulation and measurement of dynamic fiber-coupling effects for high-speed multimode VCSELs," *J. Lightwave Technol.*, vol. 23, pp. 2318–2330, 2005.

[72] J. A. Lehman, R. A. Morgan, M. K. Hibbs-Brenner and D. Carlson, "High-frequency modulation characteristics of hybrid dielectric/AlGaAs mirror singlemode VCSELs," *Electron. Lett.*, vol. 31, pp. 1251−1252, 1995.

[73] K. L. Lear, A. Mar, K. D. Choquette, S. P. Kilcoyne, R. P. Schneider Jr., and K. M. Geib, "High-frequency modulation of oxide-confined vertical cavity surface emitting lasers," *Electron. Lett.*, vol. 32, pp. 457–458, 1996.

[74] E. Yablonovitch and E. O. Kane, "Band structure engineering of semiconductor lasers for optical communications," *J. Lightwave Technol.*, vol. 6, pp. 1292−1299, 1988.

[75] T. R. Chen, B. Zhao, L. Eng, Y. H. Zhuang, J. O'Brien, and A. Yariv, "Very high modulation efficiency of ultralow threshold current single quantum well InGaAs lasers," *Electron. Lett.*, vol. 29, pp. 1525−1526, 1993.

[76] PICS3D Version 2005.11 by Crosslight Software, Inc., Burnaby, Canada. (http://www.crosslight.com)

[77] W. X. Zou, J. L. Merz, R. J. Fu, and C. S. Hong, "Very-low-threshold, strained $In_yGa_{1-y}As$-GaAs quantum-well lasers defined by impurity-induced disordering," *IEEE Photon. Technol. Lett.*, vol. 3, pp. 400–402, 1991.

[78] O. Tadanaga, K. Tateno, H. Uenohara, T. Kagawa, and C. Amano, "An 850-nm InAlGaAs strained quantum-well vertical-cavity surface-emitting laser grown on GaAs (311)B substrate with high-polarization stability," *IEEE Photon. Technol. Lett.*, vol. 12, pp. 942–944, 2000.

[79] J. Ko, E. R. Hegblom, Y. Akulova, B. J. Thibeault, and L. A. Coldren, "Low-threshold 840-nm laterally oxidized vertical-cavity lasers using AlInGaAs–AlGaAs strained active layers," *IEEE Photon. Technol. Lett.*, vol. 9, pp. 863–865, 1997.

[80] J. Ko, E. R. Hegblom, Y. Akulova, N. M. Margalit, and L. A. Coldren, "AlInGaAs/AlGaAs strained-layer 850 nm vertical-cavity lasers with very low thresholds," *Electron. Lett.*, vol. 33, pp. 1550–1551, 1997.

[81] Y.-A. Chang, J.-R. Chen, H.-C. Kuo, Y.-K. Kuo, and S.-C. Wang, "InAlGaAs/AlGaAs active region of 850-nm vertical-cavity surface-emitting lasers," *J. Lightwave Technol.*, vol. 24, pp. 536–543, 2006.

[82] R. G. Waters, R. J. Dalby, J. A. Baumann, J. L. De Sanctis, and A. H. Shepard, "Dark-line-resistant diode laser at 0.8 μm comprising InAlGaAs strained quantum well," *IEEE Photon. Technol. Lett.*, vol. 3, pp. 409–411, 1991.

[83] C. A. Wang, J. N. Walpole, H. K. Choi, and L. J. Missaggia, "AlInGaAs-AlGaAs strained single-quantum-well diode lasers," *IEEE Photon. Technol. Lett.*, vol. 3, pp. 4–5, 1991.

[84] H. K. Choi, C. A. Wang, D. F. Kolesar, R. L. Aggarwal, and J. N. Walpole, "High-power, high-temperature operation of AlInGaAs-AlGaAs strained single-quantum-well diode lasers," *IEEE Photon. Technol. Lett.*, vol. 3, pp. 857–859, 1991.

[85] N. A. Hughes, J. C. Connolly, D. B. Gilbert, and K. B. Murphy, "AlInGaAs/AlGaAs strained quantum-well ridge waveguide lasers grown by metalorganic chemical vapor deposition," *IEEE Photon. Technol. Lett.*, vol. 4, pp. 113–115, 1992.

[86] S. L. Yellen, R. G. Waters, A. H. Shepard, J. A. Baumann, and R. J. Dalby, "Reliability of InAlGaAs strained-quantum-well lasers operating at 0.81 μm," *IEEE Photon. Technol. Lett.*, vol. 4, pp. 829–831, 1992.

[87] T. E. Sale, C. Amamo, Y. Ohiso, and T. Kurokawa, “Using strained $(Al_xGa_{1-x})_yIn_{1-y}As_zP_{1-z}$ system materials to improve the performance of 850 nm surface- and edge-emitting lasers,” *Appl. Phys. Lett.*, vol. 71, pp. 1002–1004, 1997.

[88] J. Minch, S. H. Park, T. Keating, and S. L. Chuang, “Theory and experiment of $In_{1-x}Ga_xAs_yP_{1-y}$ and $In_{1-x-y}Ga_xAl_yAs$ long-wavelength strained quantum-well lasers,” *IEEE J. Quantum Electron.*, vol. 35, pp. 771–782, 1999.

[89] J. R. Jensen and J. M. Hvam, “Optical properties of InAlGaAs quantum wells: influence of segregation and band bowing,” *J. Appl. Phys.*, vol. 86, pp. 2584–2589, 1999.

[90] D. Ahn and S.-L. Chuang, “Optical gain and gain suppression of quantum-well lasers with valence band mixing,” *IEEE J. Quantum Electron.*, vol. 26, pp. 13–24, 1990.

[91] J. C. L. Yong, J. M. Rorison, and I. H. White, “1.3-μm quantum-well InGaAsP, AlGaInAs, and InGaAsN laser material gain: a theoretical study,” *IEEE J. Quantum Electron.*, vol. 38, pp. 1553–1564, 2002.

[92] W. J. Fan, S. T. Ng, and S. F. Yoon, “Effects of tensile strain in barrier on optical gain spectra of GaInNAs/GaAsN quantum wells,” *J. Appl. Phys.*, vol. 93, pp. 5836–5838, 2003.

[93] W. W. Chow, E. D. Jones, N. A. Modine, A. A. Allerman, and S. R. Kurtz, “Laser gain and threshold properties in compressive-strained and lattice-matched GaInNAs/GaAs quantum wells,” *Appl. Phys. Lett.*, vol. 75, pp. 2891–2893, 1999.

[94] P. J. A. Thijs, L. F. Tiemijer, P. I. Kuindersma, J. J. M. Binsma, and T. van Dongen, “High performance of 1.5 μm wavelength InGaAs-InGaAsP strained quantum-well lasers and amplifiers,” *IEEE J. Quantum Electron.*, vol. 27, pp. 1426–1438, 1991.

[95] P. J. A. Thijs, L. F. Tiemijer, J. J. M. Binsma, and T. van Dongen, “Progress in long-wavelength strained-layer InGaAs(P) quantum-well

semiconductor lasers and amplifiers, "*IEEE J. Quantum Electron.*, vol. 30, pp. 477–499, 1994.

[96] N. Tansu, D. Zhou, and L. J. Mawst, "Low-temperature sensitive, compressively strained InGaAsP active (λ = 0.78–0.85 μm) region diode lasers," *IEEE Photon. Technol. Lett.*, vol. 12, pp. 603–605, 2000.

[97] H. C. Kuo, Y. S. Chang, F. Y. Lai, T. H. Hsueh, L. H. Laih, and S. C. Wang, "High-speed modulation of 850 nm InGaAsP/InGaP strain-compensated VCSELs," *Electron. Lett.*, vol. 39, pp. 1051–1053, 2003.

[98] Y.-H. Chang, H. C. Kuo, F.-I. Lai, Y.-A. Chang, C. Y. Lu, L. H. Laih, and S. C. Wang, "Fabrication and characteristics of high-speed oxide-confined VCSELs using InGaAsP–InGaP strain-compensated MQWs," *J. Lightwave Technol.*, vol. 22, pp. 2828–2833, 2004.

[99] Y.-H. Cho, K.-S. Kim, S.-W. Ryu, S.-K. Kim, B.-D. Choe, and H. Lim, "Determination of the conduction-band discontinuities of $In_{0.5}Ga_{0.5}P/In_{1-x}Ga_xAs_{1-y}P_y$ by capacitance–voltage analysis," *Appl. Phys. Lett.*, vol. 66, pp. 1785–1787, 1995.

[100] Y.-H. Cho, B.-D. Choe, and H. Lim, "Band offset transitivity in AlGaAs/InGaP/InGaAsP heterostructures on a GaAs substrate," *Appl. Phys. Lett.*, vol. 69, pp. 3740–3742, 1996.

Appendix A. Publication List

1. Yen-Kuang Kuo, Sheng-Horng Yen, and **Jun-Rong Chen**, 2006, Ultraviolet Light-Emitting Diodes, in Nitride Semiconductor Devices: Principles and Simulation (Chapter 15), edited by Joachim Piprek, to be published by Wiley-VCH, the German branch of Wiley & Sons.
2. **Jun-Rong Chen** and Yen-Kuang Kuo, Accepted 16 February 2006, "Optical gain and threshold properties of strained InGaAlAs/AlGaAs quantum wells for 850-nm vertical-cavity surface-emitting lasers", to be published in Optics Communications. (SCI) (EI)
3. Yi-An Chang, **Jun-Rong Chen**, Hao-Chung Kuo, Yen-Kuang Kuo, and Shing-Chung Wang, January 2006, "Theoretical and experimental analysis on InAlGaAs/AlGaAs active region of 850-nm vertical-cavity surface-emitting lasers", Journal of Lightwave Technology, Vol. 24, No. 1, pp. 536-543. (SCI) (EI)
4. Yen-Kuang Kuo and **Jun-Rong Chen**, 2006, "Optical gain and threshold properties of strained InGaAsP/InGaP quantum wells for 850-nm vertical-cavity surface-emitting lasers", 即將投稿至 Applied Physics B: Lasers and Optics. (SCI) (EI)
5. Yi-An Chang, Tsung-Hsine Ko, Fang-I Lai, **Jun-Rong Chen**, Chun-Lung Yu, I-Tsung Wu, Hao-Chung Kuo, Tin-Chang Lu, Yen-Kuang Kuo, Li-Wen Laih, Li-Horng Laih, and Shing-Chung Wang, 2006, "Carrier blocking effect on 850-nm InAlGaAs/AlGaAs vertical-cavity surface-emitting lasers," 即將投稿至 Semiconductor Science and Technology. (SCI) (EI)
6. Yen-Kuang Kuo, **Jun-Rong Chen**, Ming-Yung Jow, Cheng-Zu Wu, Bao-Jen Pong, and Chii-Chang Chen, January 2006, "Optimization of oxide-confinement and active layers for high-speed 850-nm VCSELs", Proceedings of SPIE (Vertical-Cavity Surface-Emitting Lasers X), paper 6132-23. (EI)
7. Shu-Hsuan Chang, Yung-Cheng Chang, Cheng-Hong Yang, **Jun-Rong Chen**, and Yen-Kuang Kuo, January 2006, "Numerical simulation of optical and electronic properties for multilayer organic light-emitting diodes and its application in engineering education", Proceedings of SPIE (Light-Emitting Diodes: Research, Manufacturing, and Applications X), paper 6134-26. (EI)
8. Yen-Kuang Kuo, Sheng-Horng Yen, and **Jun-Rong Chen**, October 2006, "Numerical simulation of InAlGaN ultraviolet light-emitting diodes", 投稿至 Proceedings of SPIE (Optoelectronic Devices: Physics, Fabrication, and Application III). (EI)
9. Shu-Hsuan Chang, **Jun-Rong Chen**, Chung-Hsien Lee, and Cheng-Hong Yang,

October 2006, "Effects of built-in polarization and carrier overflow on InGaN quantum-well lasers with AlGaN or InAlGaN electronic blocking layers" 投稿至 Proceedings of SPIE (Optoelectronic Devices: Physics, Fabrication, and Application III). (EI)

10. Yi-An Chang, C.-C. Kao, Hao-Chung Kuo, J.-T. Chu, **Jun-Rong Chen**, Sheng-Horng Yen, C.-L. Yu, I. T. Wu, F. I. Lai, Tin-Chang Lu, Yen-Kuang Kuo, and Shing-Chung Wang, May 2006, "Growth and fabrication of p-side-down InGaAs:Sb/GaAs vertical-cavity surface-emitting lasers," 13th International Conference on Metal Organic Vapor Phase Epitaxy (ICMOVPE-XIII).
11. **Jun-Rong Chen**, Chung-Hsien Lee, Chien-Fang Chiu, Yen-Kuang Kuo, Bo-Ting Liou, 2005, "Starined InGaAlAs/AlGaAs active layers for 850-nm VCSELs", 2005 年台灣光電科技研討會, paper PA-FR1-073, OPT'2005 Proceedings.
12. **Jun-Rong Chen**, Jyh-Lih Wu, and Yen-Kuang Kuo, 2005, "Effect of doped GaN barrier layer on the optical and transport properties of InGaN/GaN multiple quantum-well light-emitting diodes", 2005 年中華民國物理年會, paper PD-15.
13. 吳志力、陳俊榮、郭艷光、劉柏挺, 2004, "自動脈衝式 780-nm 砷化鋁鎵雷射特性之模擬與分析", 2004 年台灣光電科技研討會, paper A-SA-II 2-5, OPT'04 Proceedings.
14. 張永政、楊政鴻、陳俊榮、郭艷光、劉柏挺、王禹文, 2004, "ITO/TPD/Alq_3/Al 有機發光二極體之模擬與特性探討", 2004 年台灣光電科技研討會, paper A-SU-II 8-4, OPT'04 Proceedings.
15. 陳秀芬、蔡孟倫、屠嫚琳、陳俊榮、郭艷光、劉柏挺, 2003 年 8 月, "短程光纖通信用紅光面射型雷射的設計與分析", 台灣光通訊產業聯盟 2003 年光通訊特刊, 第 66 至 76 頁.
16. 陳俊榮、屠嫚琳、朱漢義、郭艷光、劉柏挺, 2003, "應力與氧化層結構對磷化鋁鎵銦 650 nm 面射型雷射的影響", 2003 年台灣光電科技研討會, paper PA2-17, OPT'03 Proceedings III, pp. 110-112.
17. 楊勝州、張詒安、顏勝宏、黃詩瑋、蔡孟倫、劉冠良、陳俊榮、林漢威、何依萍、郭艷光, 2002, "紫光氮化銦鎵面射型半導體雷射之設計與分析", 2002 年台灣光電科技研討會, paper PA-33, OPT'02 Proceedings III, pp. 97-99.
18. 陳俊榮、張永政、劉柏挺、郭艷光, 2004 年 8 月, "光電半導體與 OLED 發展現況", 光訊(Opto News & Letters)邀稿, 但因雜誌停刊未發表.